Chapter 3

Optical Testing

This chapter discusses four new techniques developed for testing different optical parameters. Section 3.1 describes a technique for testing collimation using optically active medium. The remaining sections deal with testing of refractive index of thin convex lenses, linear dichroic sheet polarizers and beamsplitters using Michelson Interferometer as basic setup.

3.1 Collimation testing utilizing optically active materials

Test for collimation is very important in optical experiments. Many methods for testing the collimation of a laser beam have been developed. These methods include techniques utilizing interferometry and self imaging[77]-[83]. In the interferometric techniques, the incident wavefront is split into two and they are made to interfere. The space where interference occurs will contain some fringes. These fringes contain the information about the collimation of the interfering beams. An analysis of these fringes yields required information about collimation[77]-[79]. In self-imaging techniques, a grating is placed in the path of the test beam, which in turn produces its self-images at several planes (self-imaging planes) perpendicular to the direction of propagation. By placing a grating identical to the original one at self-imaging planes, moiré fringes can be observed. The variation in the self image fringes gives

the amount decollimation/collimation[80]-[84]. In all the above mentioned techniques a referencing or a visual inspection and analysis of the images are necessary to determine collimation.

Recently a method to image 3D wavefronts was developed utilizing a birefringent plate[84]. The output intensity caused by a plane polarized wavefront passing through a birefringent plate placed between a pair of crossed polarizers depends upon the distance each portion of the wavefront traveled through the birefringent medium because of the change in rotation of the plane of polarization. Therefore wavefronts traveling more distance will produce more output intensity and vice-versa The same principle applies for optically active materials. The property of the optically active medium to rotate the plane of polarization of the incident plane polarized light along with the change in the distance traveled inside the active medium by different wavefronts (diverging, converging or collimated) is utilized to determine the collimation of the wavefront. This method does not require fringe referencing or analysis, is free from stringent optical requirements of interferometric methods and yields accurate results.

3.1.1 Experimental setup and Theory

The collimation testing is realized utilizing the optical setup shown in Fig. 3.1. Light from a He-Ne laser source (S) (632 8nm, 30mW) is expanded using a spatial filtering assembly (SF) consisting of a microscopic objective (MO) and a pin hole placed at the focal point of the objective. The diverging beam from the pin hole falls on the collimating lens (CL) (lens under test) The collimating lens is mounted on a translation stage having least count of 0.01 mm. The collimating lens can be moved along the optic axis, making it possible to introduce a known amount of decollimation/defocusing. The beam after passing through a stop (D) which reduces the beam size to 20 mm, falls on the polarizer (P). The polarized beam then passes through the optically active medium (OAM) (quartz rotators of 22.5^o and 45^o rotations at 632.8nm), and an analyzer (A), which is a polarizer with its plane of polarization perpendicular to that of P. The output from the analyzer is gathered by a concentrating lens (L1) and is measured using a photodiode (PD) and an amplifier. The amplification unit (AU)

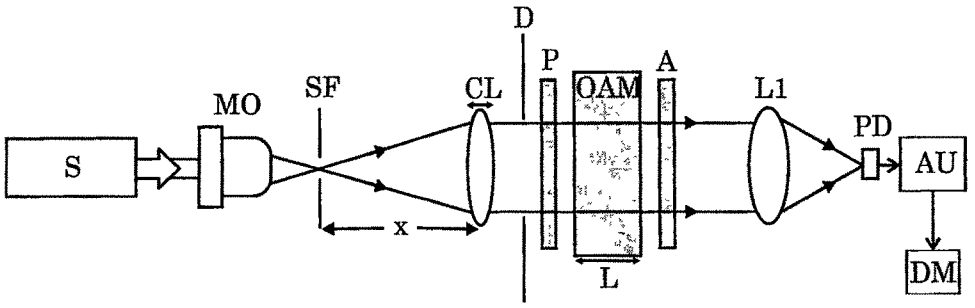

Figure 3.1: Experimental setup

consists of a current-voltage amplifier and a differential amplifier. The output from the amplifier was measured using a sensitive digital meter (DM). The OAM is an optically active medium which normally rotates the plane of polarization of linearly polarized light passing through it[5]. Linearly polarized light can be considered to be composed of two circularly polarized waves, one right circularly polarized and other left circularly polarized. The linearly polarized light entering the optically active medium is decomposed into its constituents, which travel through the medium with different velocities (because of different refractive indices for left and right circular polarizations). This will result in a phase difference between the two waves at the exit face of the optically active medium. After coming out of the medium, these waves will recombine to form a linearly polarized beam with its plane of polarization rotated, making the plane of polarization of the linearly polarized light no longer perpendicular to the plane of polarization of the analyzer (Fig. 3.2).

The amount of rotation of the plane of polarization for a normal incident beam is given by[5]

$$\beta = \rho L \tag{3.1}$$

where ρ is specific rotation (rotation of plane of polarization caused by unit length of the medium) and L is the thickness of the crystal respectively. The specific rotation is given by[5]

$$\rho = \pi \left(n_l - n_r\right)/\lambda \tag{3.2}$$

where n_l and n_r are the refractive indices for left and right circularly polarized waves respectively and λ is the vacuum wavelength of the incident light. Depending on the values of n_l and n_r the output will be d-rotatory or l-rotatory.

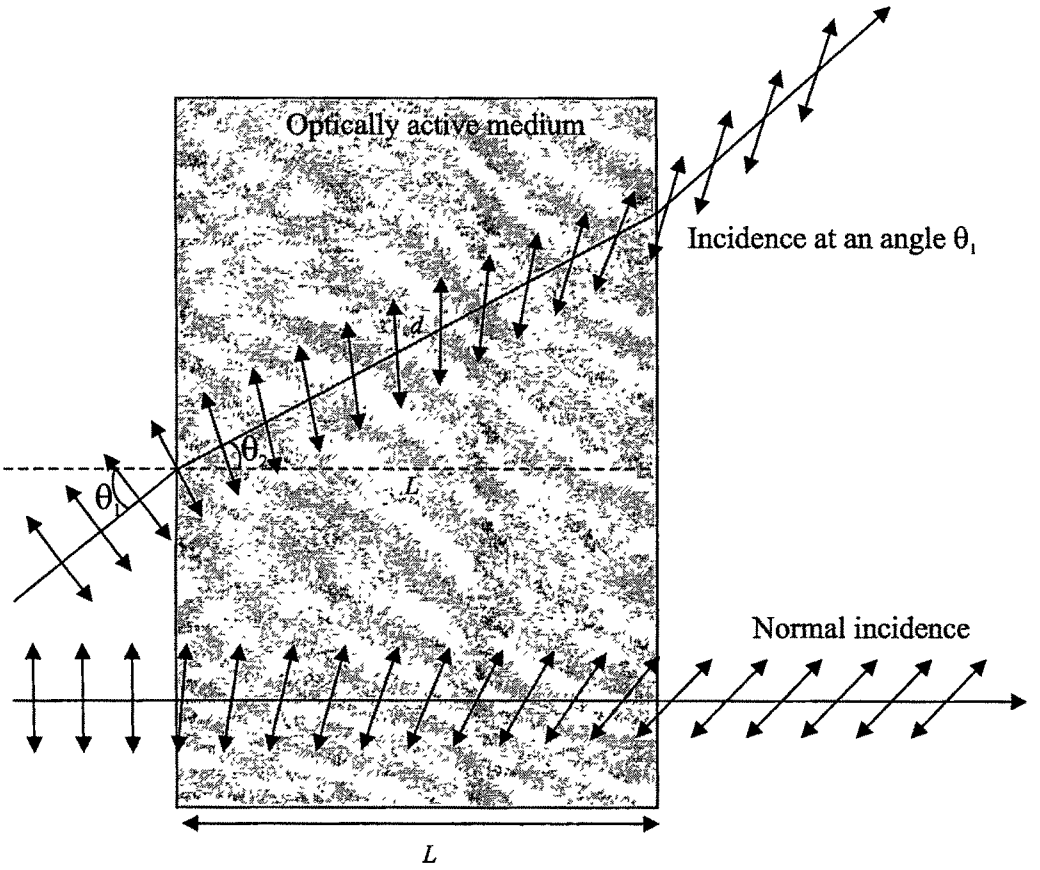

Figure 3.2: Rotation of plane of polarization caused by an optically active medium of length L to light rays incident at different angles

Quartz crystal is optically active and rotates the plane of polarization of plane polarized light when it is incident along its optic axis. Along that direction, double refraction or birefringence does not occur. *d*-rotatory quartz crystals producing 22.5° and 45° rotations (for normal incidence) at 632.8 nm having aperture sizes of 25 mm are used in the experiment.

From Eqn. (3.1) it can be seen that the rotation of the plane of polarization caused by an optically active medium having a particular specific rotation depends only upon the distance traveled by the light wave inside the medium (Fig. 3.2). For a diverging (Fig. 3.3a) or a converging (Fig. 3.3c) beam, the distances traveled are greater than that traveled by a collimated beam (Fig. 3.3b). The distance traveled by a portion of the wavefront inside the medium depends upon the incident angle it makes with

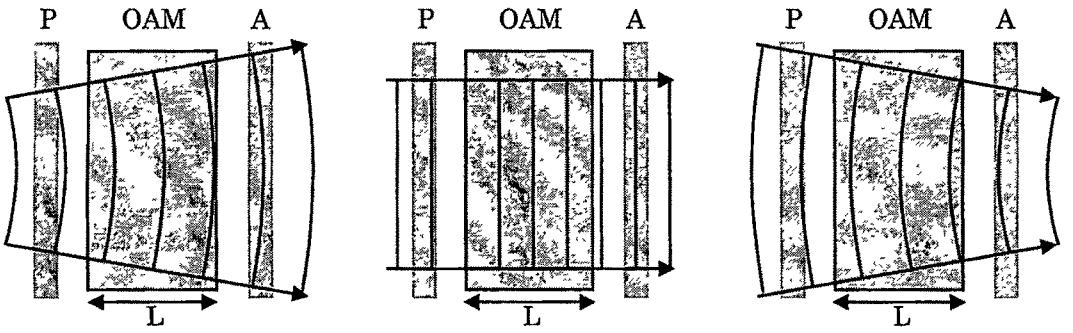

(a) Diverging wavefront (b) Collimated wavefront (c) Converging wavefront

Figure 3.3. Propagation of different wavefronts through optically active medium

the optically active medium (Fig. 3 2). It can be expressed as

$$d = \left(\frac{L}{\cos(\theta_2)}\right) \tag{3.3}$$

Where d is the distance traveled inside the medium and θ_2 is the angle of refraction which depends upon the incident angle θ_1 and refractive index of the medium. Then the rotation of plane of polarization can be written as,

$$\phi = \rho d \tag{3.4}$$

From Eqn. (3.4) it can be seen that converging or a diverging beam gives rise to higher output intensities from the analyzer due to larger rotations of the plane of polarization of the incident beam when passed through an optically active medium. This effect is utilized to find the collimation of the laser beam. When the beam is exactly collimated, it travels minimum distance inside the medium (Fig. 3.3b). Hence, when the beam is collimated the output intensity from the analyzer will be a minimum. Therefore by moving the collimating lens along its optic axis and measuring the output intensity the collimation position can be found. For the lens placed at any other position than the collimation position, the output will be greater. The output intensity from the analyzer can be calculated using Malu's law. Fig. 3.4 shows the variation in output intensity with the incident angle, which in turn depends upon the lens position. A quartz crystal giving rise to 45° rotation is considered (refractive index 1 6). From the figure it can be seen that only at collimation position the intensity is a minimum.

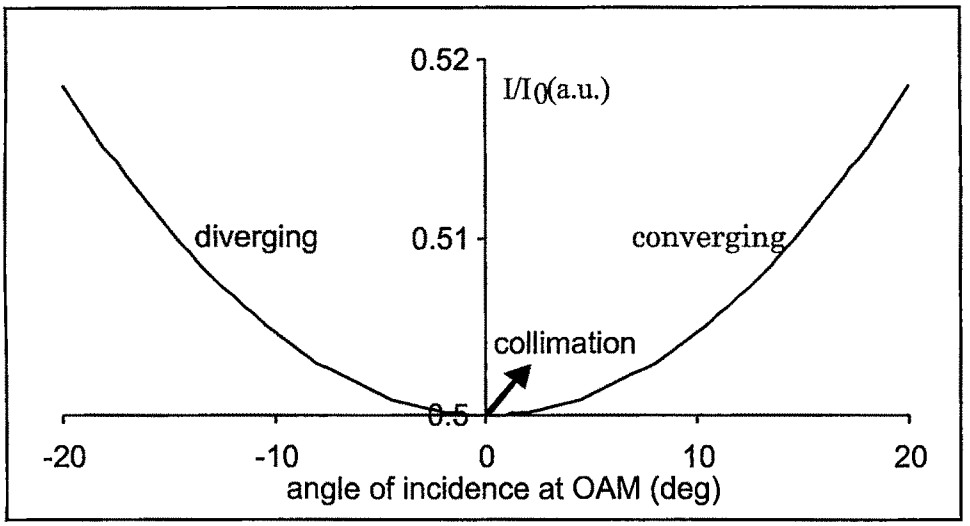

Figure 3.4: Change in output intensity with incident at the optically active medium

3.1.2 Results and Discussion

Lenses having various focal lengths are used to collimate the incident beam using the experimental setup shown in Fig 3.1. The lenses are translated along the optic axis and the corresponding output intensities are measured using the photodiode. For all the lenses used, the output intensity is found to decrease, reach a minimum and then increase as the lens is moved from inside the focus to outside the focus (this minimum is used in the differential amplifier stage). Fig. 3.5 shows the variation in the output intensity with the position of the lens from the pinhole (x) for a lens of focal length 50 mm It can be seen that the output intensity decreases as the lens is moved towards its focus and then increases as it is moved out side the focus. Fig 3.5 also shows a least square fit to the experimental data Figures 3 6 to 3.10 show the change in output intensities for lenses of focal length 100 mm, 150 mm, 200 mm, 250 mm and 300 mm respectively. It is evident from these figures that the change in output intensity with position for long focal length lenses are less compared to short focal length lenses. This can be attributed to the fact that the beam divergence for same translation distance is less for long focal length lenses.

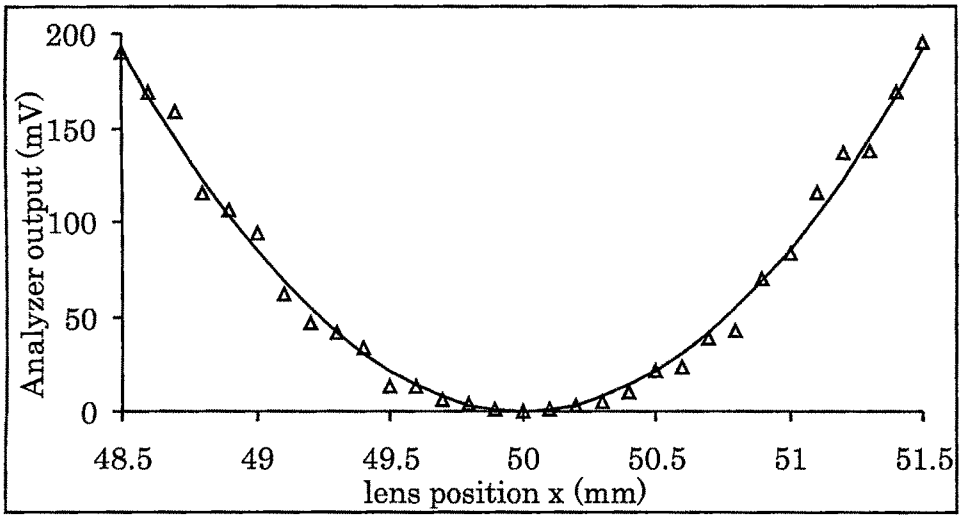

Figure 3.5: Change in normalized measured intensity with lens position for a 50 mm focal length lens (Δ· Experimental, — : least square fit)

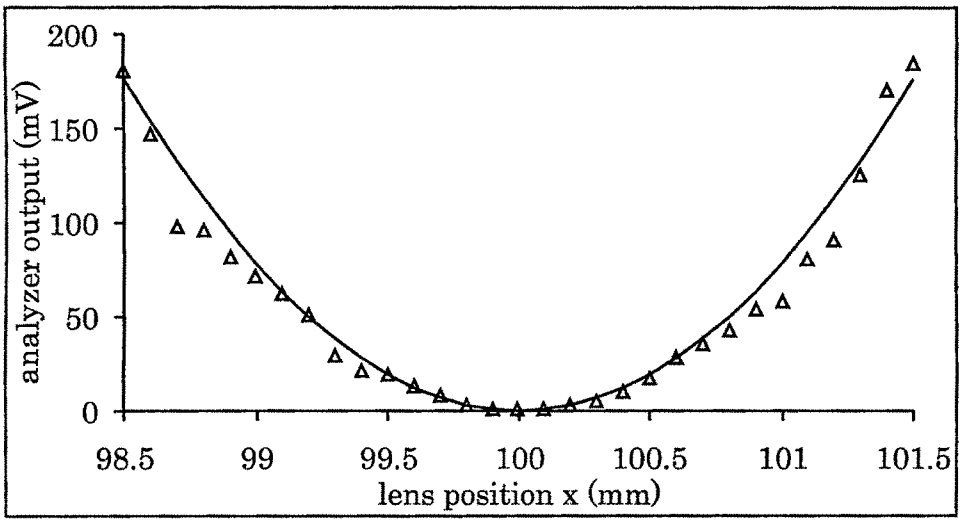

Figure 3.6: Change in normalized measured intensity with lens position for a 100 mm focal length lens (Δ. Experimental, — : least square fit)

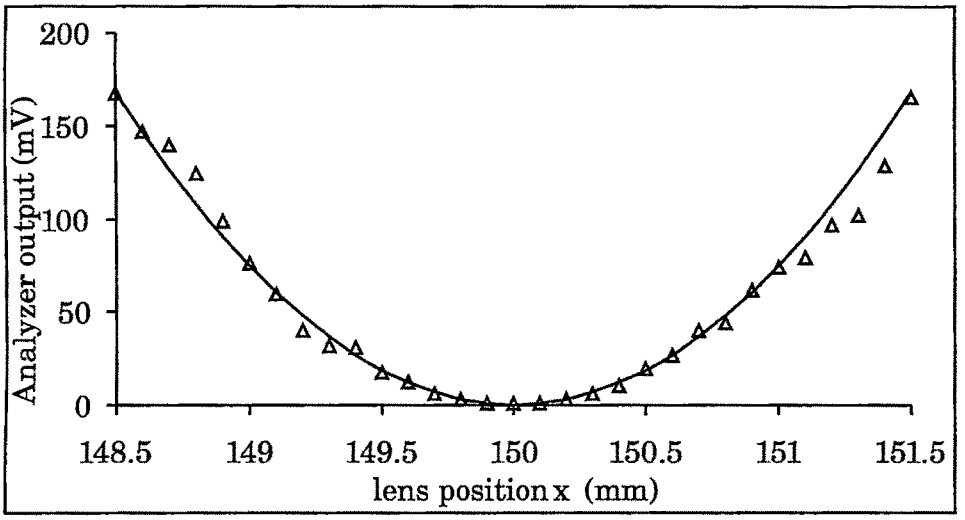

Figure 3 7: Change in normalized measured intensity with lens position for a 150 mm focal length lens (Δ: Experimental, — : least square fit)

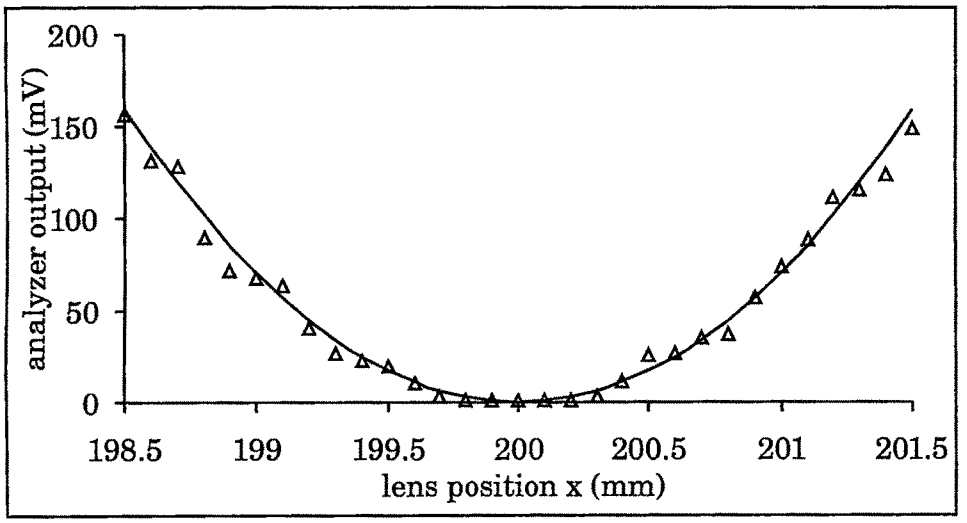

Figure 3.8 Change in normalized measured intensity with lens position for a 200 mm focal length lens (Δ: Experimental, — . least square fit)

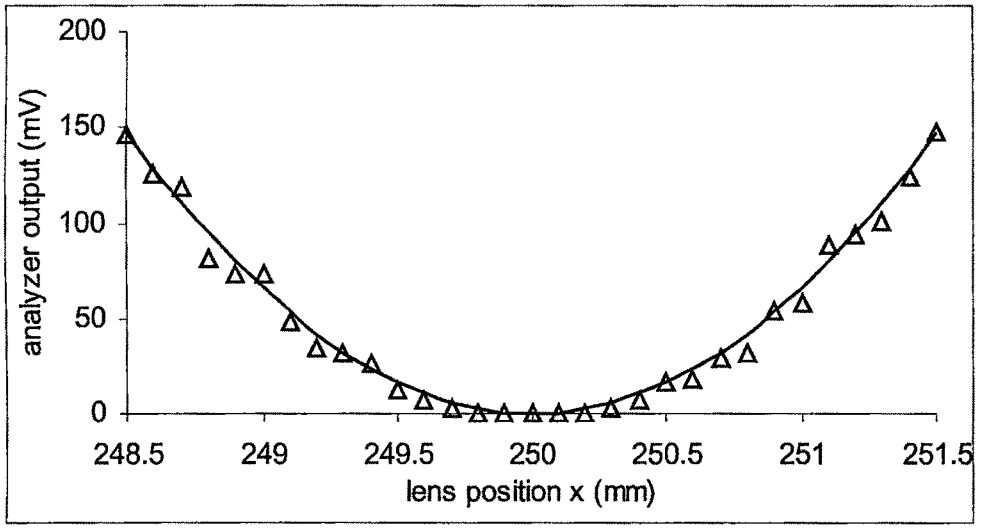

Figure 3.9: Change in normalized measured intensity with lens position for a 250 mm focal length lens (Δ: Experimental, — : least square fit)

The error in finding the collimation position or sensitivity (Δf) of the method is determined by moving the lens from on either side of the position where the output intensity is a minimum (i.e. at collimation), till the output intensity just begins to increase It is found that the sensitivity decreases with focal length. This is understandable from the fact that long focal length lenses require longer optically active mediums to produce the same amount of rotation. The change in Δf with focal length is given in Table 3.1. These values are the average of several measurements made. The change in $(\Delta f/f)\%$ is also given in the table. The Δf obtained are comparable with those using other methods[77]-[83] especially for low focal length lenses

Optically active mediums with larger rotations might give much higher sensitivity compared to the present one. The optically active rotator should be selected in such a way so that the rotation at the collimation position should always be less than when there is decollimation Another criterion should be the refractive index of the medium. In higher refractive index mediums, angle of refraction is more and hence sensitivity will be less. The sensitivity of the method will be higher if the difference of intensities between minimum rotation (normal incidence/collimation) position and other positions (converging/divergence) are large. $\Delta I/I_0 = I_\theta - I_{normal}$,

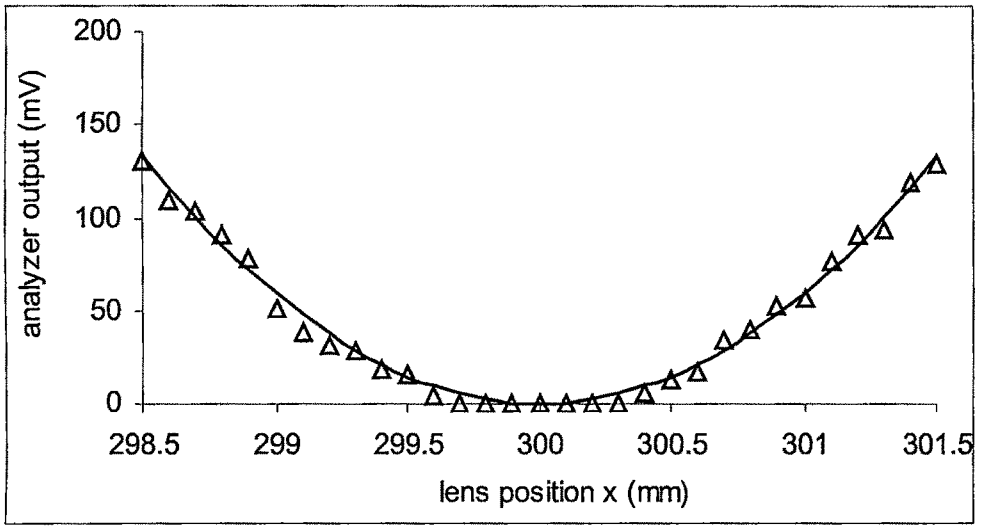

Figure 3.10: Change in normalized measured intensity with lens position for a 300 mm focal length lens (Δ: Experimental, — : least square fit)

Table 3 1. Sensitivity of the method

Focal length	Quartz crystal of 22.5° rotation		Quartz crystal of 45° rotation	
(mm)	Δf (mm)	$\Delta f/f$ %	Δf (mm)	$\Delta f/f$ %
50	0.04	0.080	0.02	0.040
100	0.09	0 090	0.06	0.060
150	0.16	0.107	0.11	0 073
200	0.22	0 110	0.20	0.100
250	0 31	0.124	0.25	0.100
300	0.36	0.120	0.31	0.103

I_θ is the output intensity for a particular angle of incidence and I_{normal} is the output intensity at collimation position For this, the crystal thickness should be optimum Fig. 3.11 shows the variation in $\Delta I/I_0$ for different incident angles (at sodium light vacuum wavelength, =21.7°). It can be seen that the maximum difference in the intensities occur for a thickness of 2.7mm. The experiment is also performed using

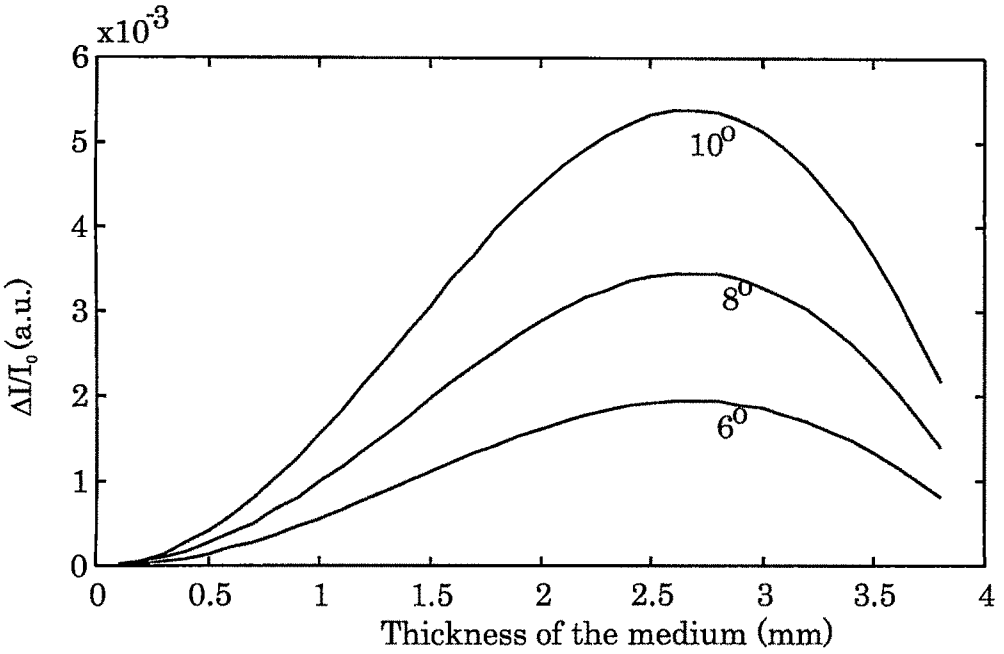

Figure 3.11: Variation of difference in intensity with medium thickness for different incident angles

photorefractive $Bi_{12}TiO_{20}$, which is not birefringent, as the optically active medium. It has a specific rotation of 6.3°/mm at 632.8 nm. Crystal having a dimension of $10\times10\times2.5$ mm^3, with the shorter dimension as the propagation direction is used. Due to the short propagation length as well as its higher refractive index, the sensitivity using BTO is found to be less. Sugar solutions having various concentrations are also used as optically active medium, but the results obtained are poor because high concentrations are necessary to obtain the desired effective rotations which in turn drastically reduces the transmission of the light beam through the medium.

3.1.3 Conclusion

It is demonstrated that the optically active materials along with a pair of crossed polarizers can be used for testing the collimation of a laser beam accurately. The method is able to provide a quantitative measurement of collimation. The sensitivity can be improved further upon by using higher optical activity medium. The method can be extended to study the aberrations in lens systems.

3.2 Study of refractive index of thin biconvex lenses using Michelson Interferometer

One of the most important factors that determine the property of optical glasses is their refractive indices and the variation of refractive index with wavelength or the dispersion[5, 85]. The knowledge of the refractive index of a particular glass material can lead to other information like its reflectance and transmittance. There are many methods to find the refractive index of a lens. The methods to determine refractive index of lenses include liquid immersion method, where a lens is immersed in a liquid whose refractive index is varied until the lens is optically visible[86]. Some of the methods depends upon the measurement of the focal length and radius of curvature of the lens by immersing the lens in liquids of different refractive indices and using Murty's shearing interferometer [87]-[91]. Measurement technique using gratings has also been reported[92]. Most of these methods use immersion of the test lens in a liquid solution making it a difficult to align and implement. In The methods using Murty's wedge plate a particular fringe pattern represents the collimation position (typically a horizontal or vertical) But to determine exactly whether the fringes are horizontal or vertical is little difficult (see Fig. 3 in Ref[94]).

Here a method to determine the refractive index of lenses and their dispersion characteristics is developed using Michelson interferometer. The Michelson Interferometer is used to find the parallelism of the incident wave front. The refractive index of thin biconvex lens is determined by measuring the focal length and radius of curvature of the lenses. The test lens itself is used as the collimating lens to determine the focal length [93]. The lens maker's formula with thin lens approximation yields accurate refractive index values. Three laser wavelengths are used to study the dispersion of the lens material The dispersion parameters of the material of the lens are found by fitting the experimental data using Sellmeier dispersion formula[4]. The dispersion curve is found to match closely with literature values[85].

3.2.1 Experimental setup and theory

When a Michelson interferometer shown in Fig 3.12 is illuminated by a point source, real non-localised interference fringes are formed in a Michelson interferometer. Fig. 3.13a shows the schematic of point source illumination of two parallel surfaces[5] (mirror M2 and image of mirror M1 i e. M1'). The rays after reflection from the two surfaces will interfere at the point of observation P. The rays can be assumed to be originating from the point sources S1 and S2 respectively as shown in Fig. 3.13a. These real non-localized fringes can be seen on a screen placed normal to the beam propagation. The path difference between the rays reaching P is given by

$$\Delta x \approx 2\,d\,\cos\,\theta \tag{3.5}$$

where d is given by

$$d = l_2 - l_1 \tag{3.6}$$

where l_2 and l_1 are the respective distances of mirrors M2 and M1 from the beam-splitter. θ is the angle made by the incident rays with the normal to the parallel surfaces. Real fringes of equal inclination are formed at the screen. Now consider Fig. 3.13b. Here the path difference between the two rays is zero ($l_2 - l_1 = d = 0$). This will produce two diverging wavefronts propagating collinearly and therefore not interfering at any point in space. A screen placed normal to the propagation of such two wavefronts, will not contain any fringes. Fig. 3.13c shows a well collimated beam reflected from mirrors M1 and M2, and propagating collinearly. Even though there is a finite path difference between the two beams reflected from M2 and M1 respectively ($l_2 - l_1 = d \neq 0$), they will not interfere at any point in space because the incident beam is well collimated. So here also no real fringes will be formed at the detector plane. This property of the Michelson interferometer is utilized to find the refractive index of convex lenses.

3.2.2 Focal length measurement

The experimental setup to measure the refractive index of thin biconvex lenses is shown in Figures 3.12 and 3 14. The beam from a laser source is expanded using a

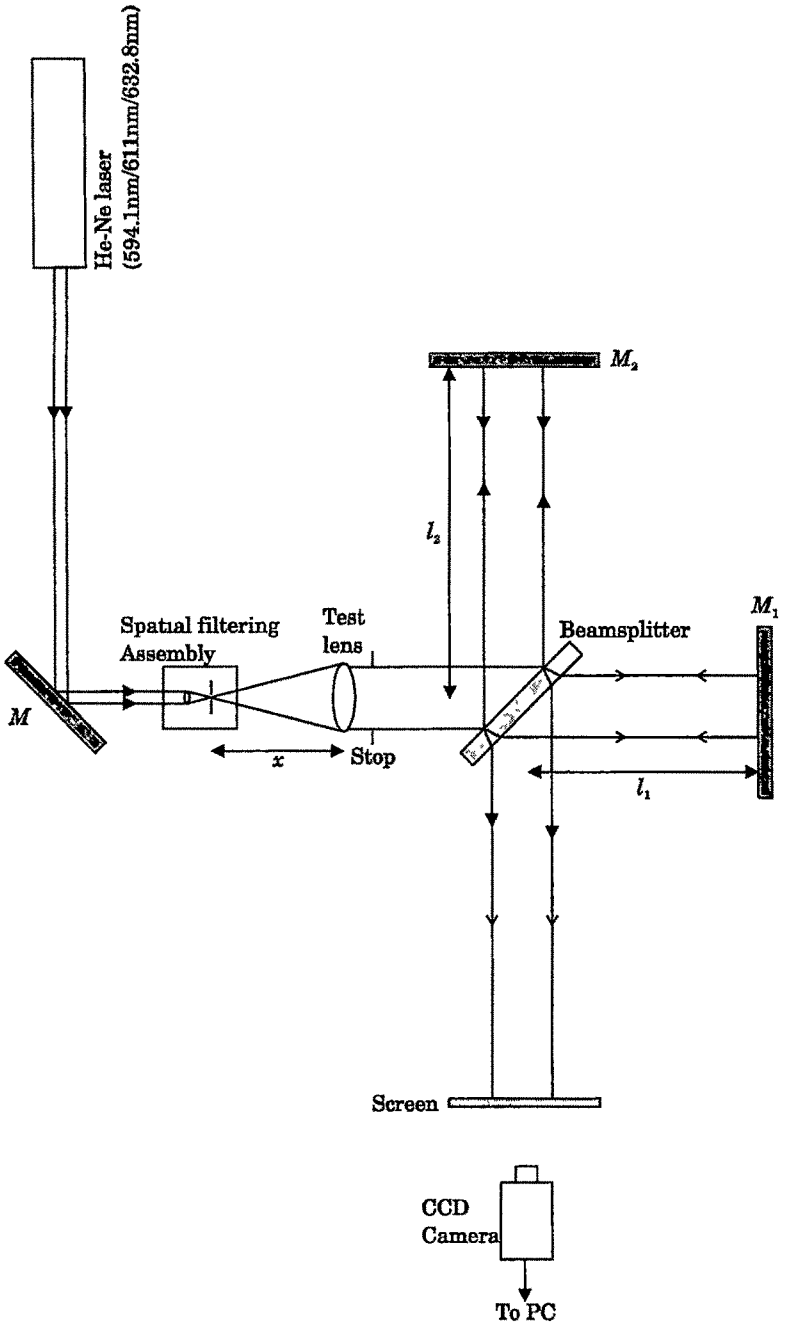

Figure 3.12: Setup for finding the focal length of a convex lens

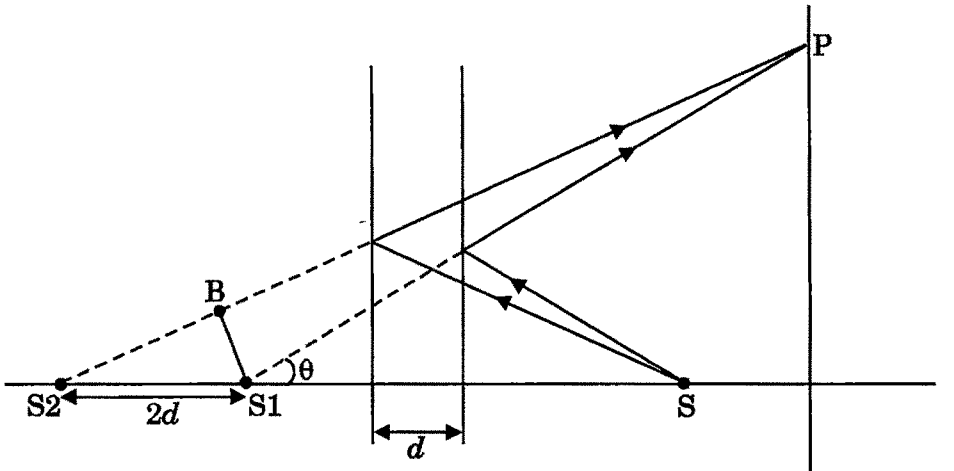

(a) Diverging wavefront with l_2-l_1=d≠0 Detector plane

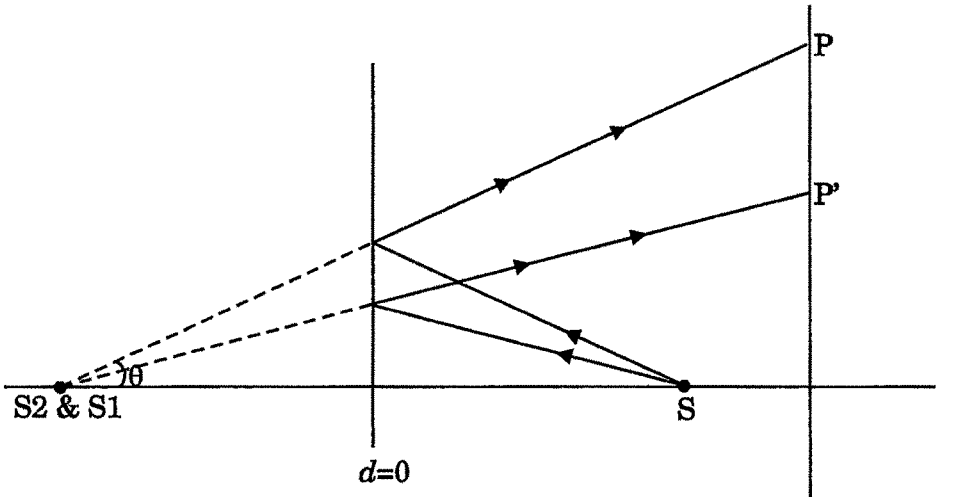

(b) Diverging wavefront illuminated with l_2-l_1=d=0 Detector plane

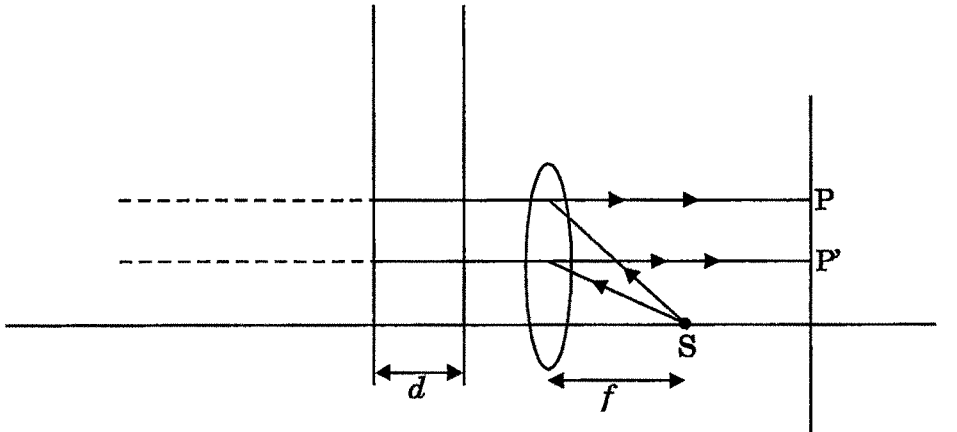

(c) Collimated wavefront with l_2-l_1=d≠0 Detector plane

Figure 3.13. Michelson interferometer with different wavefronts

spatial filtering assembly consisting of a microscopic objective and a pin hole. Three He-Ne laser sources having different wavelengths are used to determine the dispersion curve of the lens. The sources used are a 594 1 nm (yellow, 2 mW), 611 nm (orange, 2 mW) and a 632 nm (red, 10 mW). The expanded laser beam passes through the test lens (collimating lens), mounted on a lateral translation stage having a resolution of 0.01 mm. The beam is reduced in size using a stop just after the lens, to minimize spherical aberration. This beam is split into two by a 50:50 beamsplitter. The beams are reflected back by Mirrors M1 and M2. After reflections from mirrors M1 and M2 they are made to interfere at the screen. The fringe patterns are recorded on a PC using a CCD camera and frame grabber card.

Finite path length difference is kept between the two beams This condition is necessary so that there will always be formation of real fringes other than when the beams are perfectly collimated. The focal length of the test lens is measured by translating the lens along its optic axis using the translation stage. When the lens is moved along its optic axis towards the focus, the wavefront changes from diverging to collimated with the lens position Real circular fringes will be formed on the screen at every lens position (x) along the axis. These circular fringes change with the distance from the pin hole (x). The number of fringes decreases as the lens is moved towards the collimation position. When the beam is exactly collimated ($x = f$), the field of view becomes free from any fringes as there is no interference. Again after the collimation position (outside the focus), the fringes start appearing as the wavefront is converging The position where there is no real fringe is observed is the focal length of the lens.

3.2.3 Radius of curvature measurement

The schematic of the experimental setup to measure the radius of curvature is shown in Fig. 3.14 where one of the mirrors in Michelson Interferometer setup shown in Fig. 3 12 is replaced with the test lens. A well corrected lens is used to collimate the diverging beam from the pin hole The collimation is characterized by the lack of any real fringes. Along one of the arms, another good lens having a long radius of

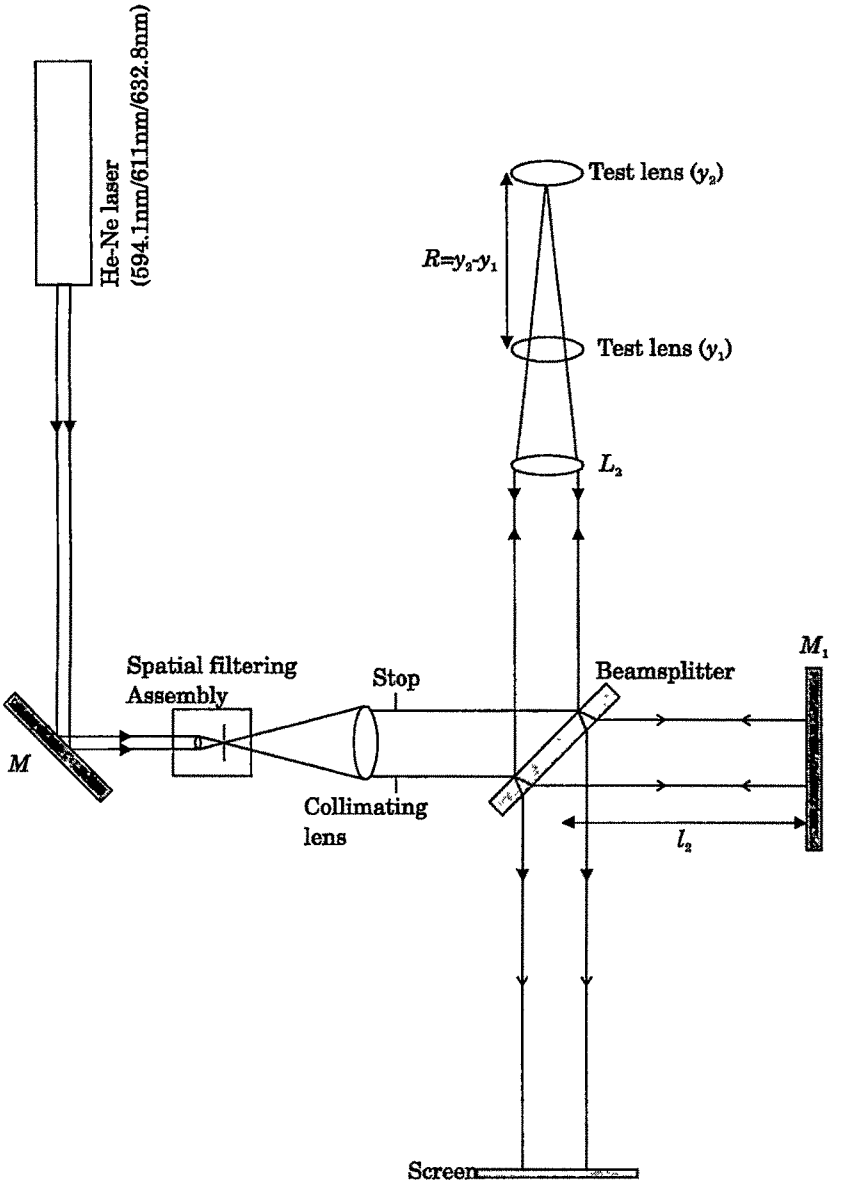

Figure 3 14: Setup for finding the radius of curvature of a convex lens

curvature was used to focus the beam on to the lens under test. The test lens was mounted on a translation stage and was moved along its optic axis Here also real circular fringes could be observed on the screen. The test lens is moved away from the focusing lens, in order to focus the light beam on the center of curvature of the front surface of the lens. At this position, the beam will become well collimated and the real fringes will disappear from the screen. This position is noted (y_1). The test lens is moved further away from the focusing lens and the circular fringes will appear again. The test lens is then moved to a position so that it coincides with the focus of the focusing lens. Here also the reflected beam from the front surface of the test lens will be collimated by the focusing lens and the real fringes will disappear from the screen. This position is also noted (y_2). The radius of curvature is given by the difference between these two positions and is

$$R = y_2 - y_1 \tag{3.7}$$

The radius of curvature of the other surface is also found using the same method.

3.2.4 Refractive index calculation

The refractive index n of the lens can be found using the lens maker's formula considering thin lens approximation. It is given by

$$n = 1 + \frac{R_1 R_2}{f\,(R_2 - R_1)} \tag{3.8}$$

where R_1 and R_2 are the radius of curvature of the two surfaces of the lens and f is its measured focal length Here R_2 is negative from the sign convention.

3.2.5 Error Analysis

The error in measurement of the refractive index dn depends upon the error dR in radius of curvature and the error df in focal length measurement. The error can be determined by differentiating Eqn. (3.4) partially with respect to R and f.

$$dn = \pm \left[\frac{dR}{2f} - \frac{R}{2f^2} df \right] \tag{3.9}$$

Substituting for R from Eqn. (3.8), one can re-write Eqn (3 9) as

$$dn = \pm \left[\frac{dR}{2f} - \frac{(n-1)}{2f} df \right] \tag{3 10}$$

For example, if f=400 mm, df = 0.14 mm and dR = 0.18 mm (all are experimental values), then the predicted error in measurement of refractive index is $dn = \pm 0\ 0002$

3.2.6 Results and discussion

To measure the refractive index and to study dispersion in lenses, three laser sources having wavelengths 632 8nm (red), 611nm (yellow) and 594 1nm (orange) respectively are used as sources in the setups shown in Figures 3.12 and 3.14. First the focal lengths of the lenses are measured using the setup shown in Fig 3 12. Biconvex lenses of various focal lengths made up of BK7 glass are used in the experiment. The path length difference $l_2 - l_1$ is kept at 5 cm. The lenses are mounted on the translation stage and the position where the real fringes disappear is determined. This gives the focal length of the lenses The obtained fringe patterns for a lens of focal length 200 mm is shown in Fig 3.15 using 632.8 nm source. The figure shows the noise removed and contrast enhanced image. It can be seen that there is no fringe in the field of view when the beam is exactly collimated

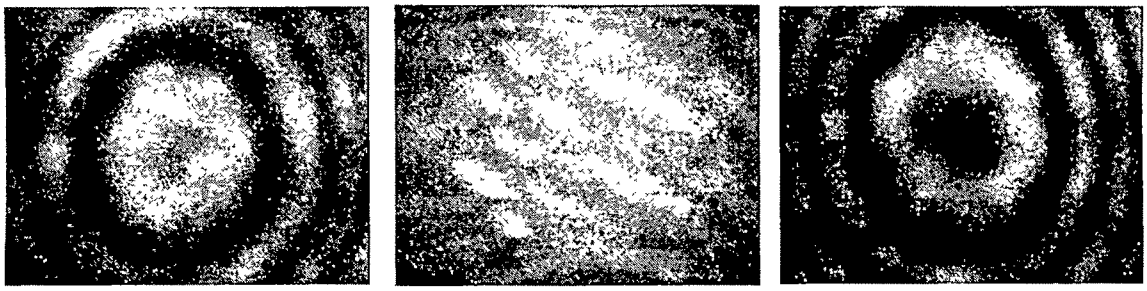

(a) x=98mm (a) x=at focus (a) x=102mm

Figure 3 15. Change in the interference pattern with lens position x for 100mm focal length lens using λ = 632.8 nm

The fringe system for a lens of 300 mm is shown in Fig. 3.16 (λ = 632 8 nm) The error in determining the collimation position (Δf) is found by disturbing the lens from the collimation position, through a minimum distance of translation over which the collimation (lack of real fringes) is observable

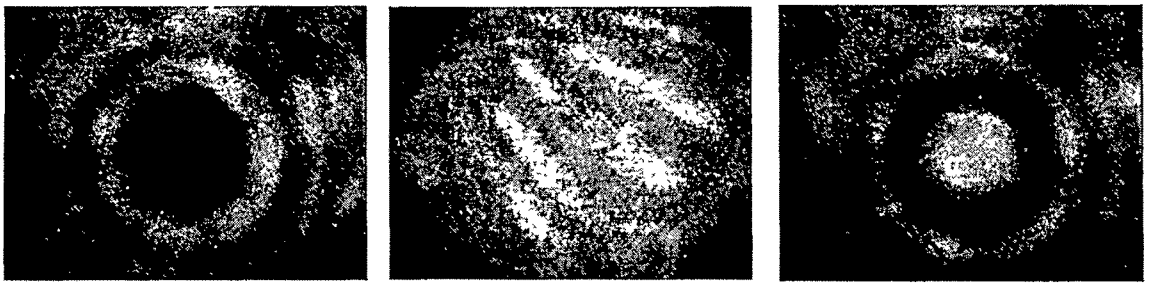

(a) x=198mm (b) x=at focus (c) x=202mm

Figure 3.16: Change in the interference pattern with lens position x for 200mm focal length lens $\lambda = 632.8$ nm

The obtained focal length values (average of several measurements) and the errors are given in Tables 3.2, 3.3 and 3.4 along with the error in measurement for different laser wavelengths. It can be seen that the error is more for long focal length lenses. This can be understood from the fact that the change in the wavefront is small for a long focal length lens than for a short focal length lens. The experiment is repeated using all the sources several times and the average of the focal length is used for the refractive index calculations.

The radius of curvatures are measured using the experimental setup shown in Fig. 3 14. A 500 mm focal length lens is used as the focusing lens. The difference in positions where there is a lack of real fringes yields the radius of curvature. The change in fringe pattern with distance of the test lens from the focusing lens (y) for a 200 mm lens is shown in Fig. 3.17. Radius of curvatures was measured using all the

Table 3.2: Measured focal length and error using 594.1 nm laser

Focal length in mm at 587.6nm light(manufacturer)	F (mm) (measured)	Δf (mm)	f (mm) (theoretical)	Deviation (mm)	% Error
200	200.14	0.04	200.10	0.04	0.02
300	300.09	0.08	300.16	0.07	0.02
400	400 07	0.12	400.21	0.14	0.03

Table 3.3. Measured focal length and error using 611 nm laser

Focal length in mm at 587.6nm light(manufacturer)	F (mm) (measured)	Δf (mm)	f (mm) (theoretical)	Deviation (mm)	% Error
200	200.42	0.05	200.36	0.06	0.03
300	300.55	0.09	300.54	0.01	0.01
400	400 54	0.12	400.72	0.18	0.05

Table 3.4: Measured focal length and error using 632.8 nm laser

Focal length in mm at 587 6nm light(manufacturer)	F (mm) (measured)	Δf (mm)	f (mm) (theoretical)	Deviation (mm)	% Error
200	200.71	0.04	200.66	0.05	0.03
300	300.92	0.08	301.00	0.08	0.03
400	401.15	0.14	401.33	0.18	0.04

sources and average was calculated. This is given in Table 3.5 along with the error in the measurement. The table also gives the radius of curvatures calculated using the manufacturers data.

Next, refractive indices are calculated using the Eqn. (3.8) and the results are given in Table 3.6. The refractive indices given in Table 3.6 are the average of several measurements. The errors are the deviation from the data given in Ref [89]. Even with the thin lens approximation accurate values for refractive indices are obtained. The refractive indices can be measured up to an accuracy of ± 0.0004. This is comparable with the results obtained with other methods[87, 91].

The change in refractive index n with wavelength λ is a straight line for all the transparent glass materials for the range of wavelengths used. This is shown in

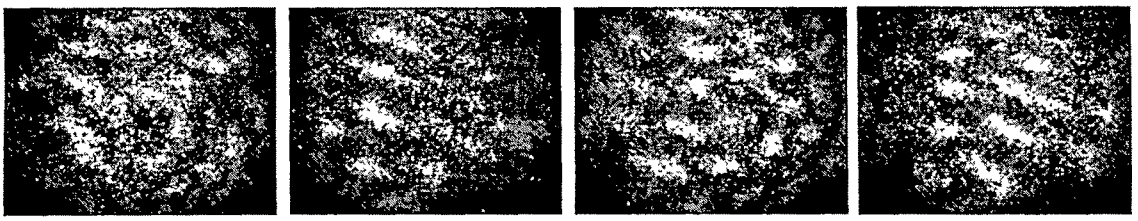

(a) y=200mm (b) y=y_1=293.39mm (c) y=400mm (d) y=y_2=500mm

Figure 3.17: Change in the interference pattern with lens position from the focusing lens y for 200 mm focal length lens using $\lambda = 632.8$ nm

Table 3.5: Measured radius of curvature and error in measurement

Focal length in mm (as specified by manufacturer)	Calculated radius of curvature from manufacturer data (mm)	Measured R (mm) R_{avg}	Deviation (mm)	% Error
200	206.72	206.59	0.13	0.06
300	310.08	310.26	0 18	0.06
400	413.44	413.61	0.17	0.04

Table 3.6: Measured refractive index and error in measurement

Focal length (mm)	Measured refractive indices and errors at various wavelengths lengths								
	λ = 594.1 nm			λ = 611 nm			λ = 632.8 nm		
	meas.	lit	Error	meas.	lit	Error	meas.	lit.	Error
200	1 51611	1.51653	0.00042	1 51539	1 51587	0.00048	1 51465	1.51509	0.00044
300	1.51694	1.51653	0 00041	1.51615	1.51587	0.00028	1.51552	1.51509	0 00043
400	1 51692	1.51653	0.00039	1.51632	1.51587	0.00045	1.51553	1 51509	0 00044

Fig. 3.18 for the Schott glass type BK7 using literature data[85]. This is true for other glass types also. Fig. 3.19 shows the change in measured refractive index with wavelength using the present method for 200 mm focal length lens. The change is

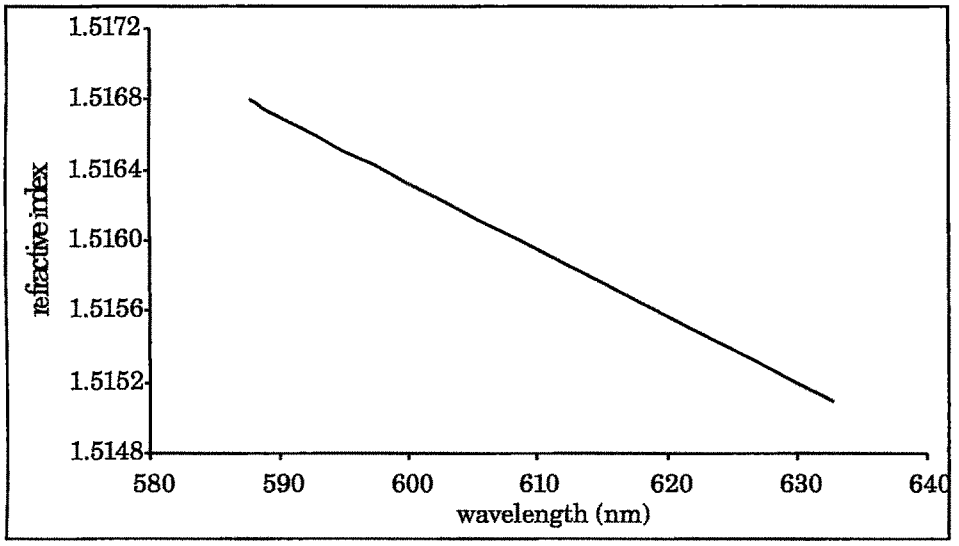

Figure 3.18: Change in refractive index with wavelength for BK7 glass for the region of interest (~580-640 nm)

linear. A linear fit to the plot is also shown. The dispersion relation of transparent materials for wavelengths in the visible and infrared region is given by the Sellmeier dispersion formula[4, 94, 95].

$$n(\lambda) = \sqrt{1 + \sum_{j=1}^{k} \frac{B_j \lambda^2}{\lambda^2 - C_j^2}} \tag{3.11}$$

where λ is the wavelength in micrometers and B's and Cs are the characteristic material constants.

For satisfactory fitting of refractive index data, $k = 3$ is sufficient for almost all materials in their main transparent region[93, 96, 97]. From the linear fit for the measured refractive index (Fig. 3.19), the dispersion constants can be determined by fitting the Sellmeier dispersion equation [94, 96, 98, 99]. The obtained dispersion constants are given in Table 3.7. The dispersion curve for BK7 glass using the measured refractive indices and calculated dispersion constant is shown in Fig. 3.20, also shown is the dispersion curve using the available data[85]. The curves closely match thus validating the results -

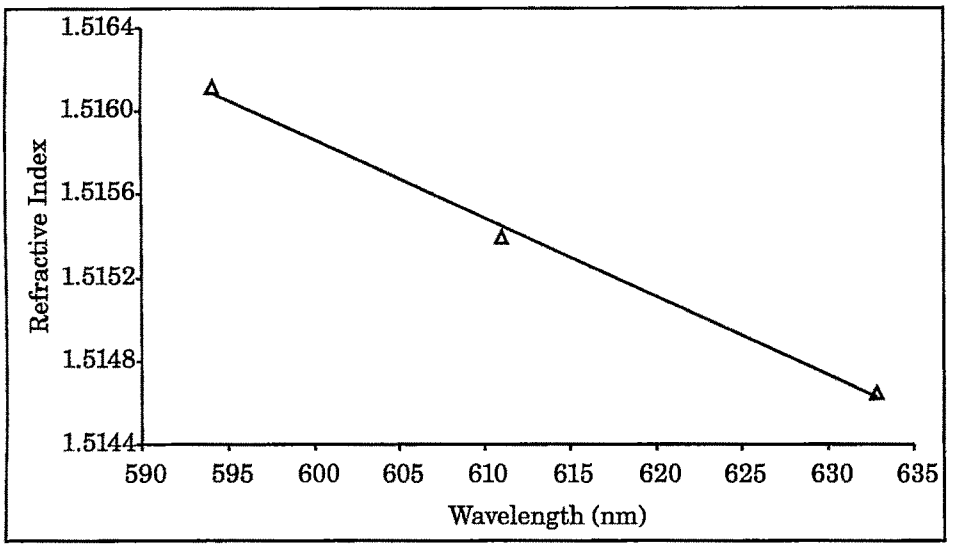

Figure 3.19· Measured change in refractive index with wavelength for BK7 glass (Δ experimental,— linear fit)

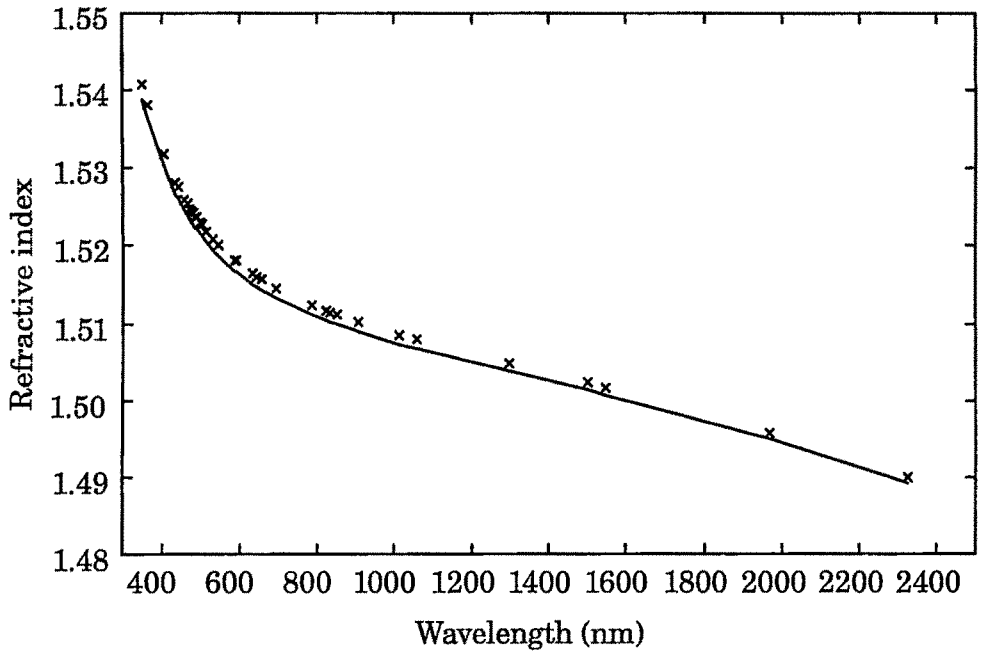

Figure 3.20. Refractive index change with wavelength for BK7 glass (× Sellmeier formula fitting, — literature)

Table 3.7: Obtained material parameters

Material Parameter	From fitting	Literature	% error
B1	1 0505729	1.0396121	1.05
B2	0.2247192	0.2317923	3.05
B3	1.0647185	1.0104695	5.37
C1	0.0056143	0.0060007	6.44
C2	0 0223143	0.0200179	11.47
C3	105.6412010	103.5606530	2.01

3.2.7 Conclusion

A method using Michelson Interferometer is developed for refractive index measurement and for studying the dispersion in thin biconvex lenses. The refractive index is found by measuring the focal length and the radius of curvature of the lens. Thin lens approximation is used for the refractive index calculation. This may introduce some error in the refractive index measurement But even with this approximation, accurate results are obtained. Using laser sources of differing wavelengths, the material parameters of the lens glass material is also determined. The dispersion curves match well with the literature data. The method can be used for other type of transparent materials also.

3.3 Testing of linear dichroic sheet polarizers with Michelson interferometer

Linear polarizers are used for producing linearly polarized light from incident unpolarized light. If natural (unpolarized) light is incident on an ideal linear polarizer, only the light in the plane, having orientation parallel to the transmission axis of the

polarizer should be transmitted The most commonly used linear sheet polarizers are based on dichroism which refers to the selective absorption of one of the two orthogonal polarization components[4, 5, 85] The dichroic polarizer is made up of anisotropic material, which strongly absorbs one of the orthogonal field components, while being transparent to the other[4, 5]. Sheet type dichroic polarizers are manufactured from organic materials by imbedding them into a plastic sheet and then stretching the plastic sheet to align the molecules and causing them to be birefringent. This is then dyed so that the dye molecules attach themselves to the aligned polymer molecules. The conduction electrons of the dye can move along the polymer chain The electric field component in the incident wave that is parallel to the molecules drives the electrons and hence does work and is therefore absorbed. The transmission axis of the polarizer is perpendicular the direction in which the film is stretched[4, 5, 85]. This type of polarizers are extensively used especially in low power and visual applications[85]. When such a pair of polarizers with perpendicular polarization directions are used, the output intensity should be zero ideally. But due to non absolute absorption of one of the orthogonal components, this quantity will always be greater than zero[100].

The parameter that determines the leakage of the absorbed component is the extinction ratio[85]. Usually the extinction ratio is determined by passing unpolarized light through a pair of polarizers having perpendicular polarization directions and measuring the output using photo-detector. But at low intensities the extinction ratio is impossible to measure using this method as the output would be immeasurable with conventional photo-detectors even with high amplification. In the case of interference, the visibility (or contrast) of the fringe system depends upon the direction of polarization of the two interfering beams also[5]. If two beams having perpendicular polarizations interfere, there will not be any fringe formation, resulting in zero visibility Any deviation from this results from the non-zero extinction ratio of the polarizers Here a method to measure the extinction ratio using Michelson interferometer is discussed. By this method the open transmittance, the polarizers can also be measured.

3.3.1 Experimental setup and Theory

The experimental setup used is shown in Fig 3 21, using Michelson interferometer geometry. A 10 mW He-Ne (632.8 nm, unpolarized, Uniphase) laser is expanded using spatial filtering (SF) assembly. This is split into two by a 50:50 beamsplitter The transmitted and reflected beams are made to interfere at the detector plane by mirrors M1 and M2 respectively. Two polarizers P_{ref} (reference polarizer) having an extinction ratio of 1×10^{-4} and P_{test} (test polarizer) are kept on the transmission and reflection arms respectively. They are kept at a small angle with the normal to the mirrors to avoid reflections from them interfering at the detector plane. The mirrors of the interferometer are adjusted to get real fringes at the detector plane. The output is measured using a photodiode mounted on a translation stage having 0.01 mm resolution. A small rectangular aperture is placed just in front of photodiode to limit its exposure area to get accurate results. The output of the detector is amplified and is measured by a sensitive digital meter. The spherical test and reference beams arriving at the detector plane can be written as

$$\vec{E_t} = \frac{\vec{E_1}}{r_1} e^{-\imath \vec{k}\, \vec{r}_1} \tag{3.12}$$

$$\vec{E_r} = \frac{\vec{E_2}}{r_2} e^{-\imath \vec{k}\, \vec{r}_2} \tag{3 13}$$

where $\vec{E_1}$ and $\vec{E_2}$ is the amplitudes of the test and reference beams respectively, $\vec{k}$ is the propagation vector and $\vec{r_1}$,$\vec{r_1}$ are the position vectors of the two wave fronts. The total intensity at the detector plane can be written as,

$$I = \left(\vec{E_r} + \vec{E_t}\right)^2 = \frac{\vec{E_1}^2}{r_1^2} + \frac{\vec{E_2}^2}{r_2^2} + \frac{2\, \vec{E_1} \cdot \vec{E_2}}{r_1\, r_2} \cos(\delta) \tag{3.14}$$

where

$$\delta = \vec{k} \cdot \vec{r_1} - \vec{k} \cdot \vec{r_2} \tag{3.15}$$

is the phase difference between the two waves reaching the detector plane. By substituting

$$I_0 = E_1^2/r_1^2 + E_2^2/r_2^2 = I_1 + I_2 \tag{3.16}$$

as the uniform illumination, the intensity equation (Eqn. (3.12)) can be re-written as[3]–[5]

$$I = I_1 + I_2 + 2\sqrt{I_1 I_2}\, \cos(\theta)\, \cos(\delta) = I_0\, (1 + V\, \cos(\delta)) \tag{3 17}$$

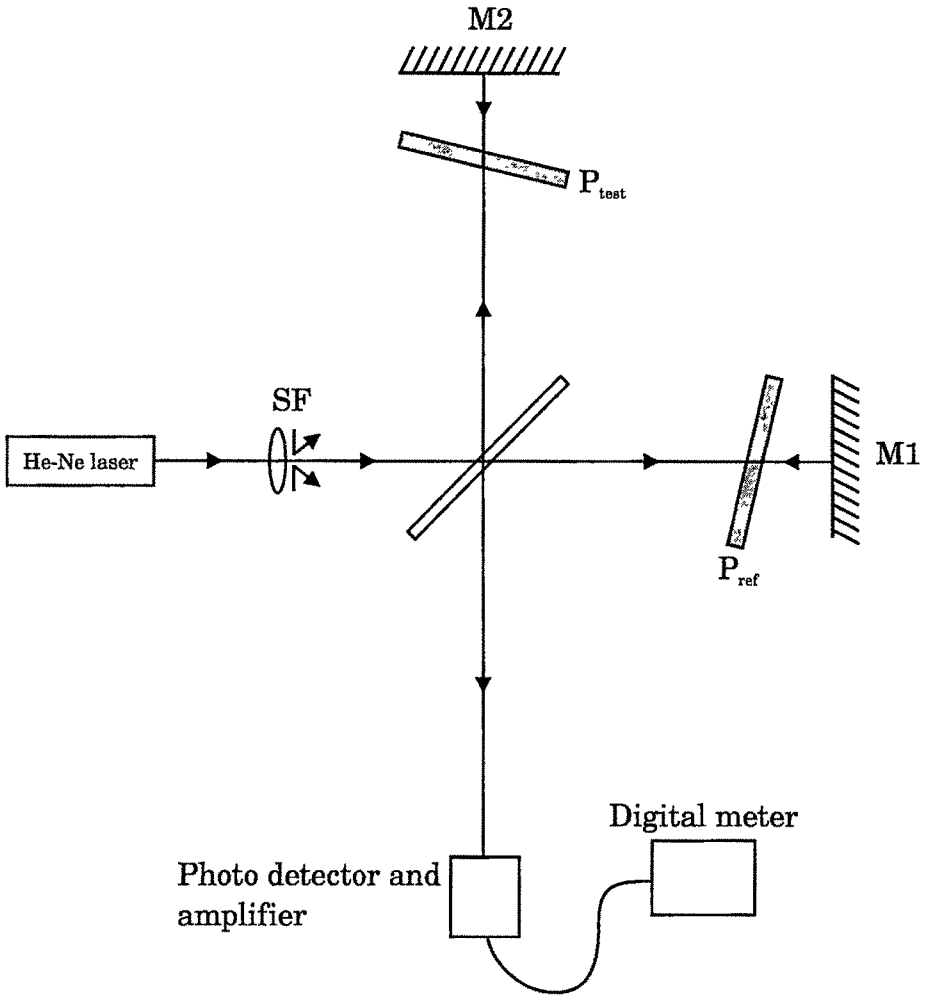

Figure 3.21: Experimental setup for testing of linear polarizers

where

$$V = \frac{I_{max} - I_{min}}{I_{max} + I_{min}} = \frac{2\sqrt{I_1 I_2}}{I_1 + I_2} \cos(\theta) = M \cos(\theta) \tag{3.18}$$

is the visibility of the interference fringes with θ as the angle between the plane of polarization of the two interfering beams. From Eqn. (3.18) it can be seen that as θ increases, the visibility of the interference fringes decreases, reaching zero when $\theta = 90^o$ The variation in visibility (V) with the angle between the planes of polarizations of two interfering beams (θ) is shown in Fig. 3.22. The range of θ is chosen from 0^o to 360^o corresponding to a full rotation of the polarizer. From Fig. 3.22 it can be seen that if the polarization states of any one of the interfering beams is changed, then the visibility also changes Therefore visibility can be used as a parameter to test linear polarizers.

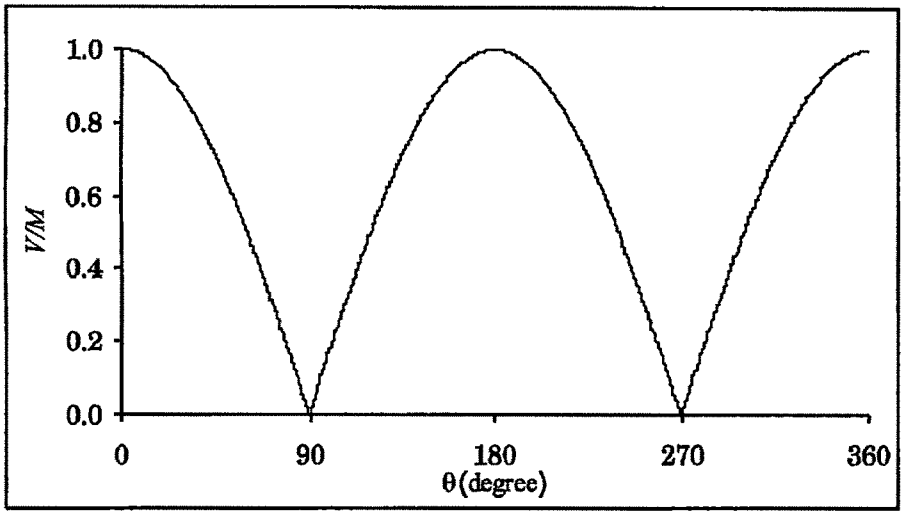

Figure 3.22 Visibility of the interference fringes for different angle between the polarizers

The extinction ratio of a pair of polarizers is defined as the transmission of the pair when the polarizers have perpendicular polarization direction[85]. An ideal polarizer pair should have an extinction ratio of zero. But due to non-absolute absorption of the desired orthogonal component, it will always be greater than zero. If the relative intensity between the interfering beams is kept a constant then the visibility of the interference fringes depends only on the state of polarization of the beams. So by rotating one of the polarizers, the minimum (V_{min}) and maximum (V_{max}) visibility can be determined Maximum visibility corresponds to $\theta = 0^o$ and minimum visibility corresponds to $\theta = 90^o$ The transmittance of a dichroic polarizer for a linearly polarized incident beam is given by[85]

$$T = a_1 \cos^2\theta + a_2 \sin^2\theta \tag{3.19}$$

where θ is the angle between the plane of polarization of incident light and the polarizer, a_1 and a_2 are the principal transmittance of the polarizer. Ideally $a_1 = 1$ and $a_2 = 0$ (there is no transmittance when $\theta = 90^o$) But practically a_1 is always greater than 1 and a_2 always has some finite value[85]. If the incident beam is unpolarized as in the present case, angle is defined as the angle between the planes of polarizations of the pair of polarizers. Transmittance of such pair of polarizers is given by[85]

$$T_{pair} = \frac{1}{2}\left[a_1 a_2 \sin^2(\theta) + \frac{1}{2}\left(a_1^2 + a_2^2\right)\cos^2(\theta)\right] \tag{3.20}$$

This equation takes into account the fact that the interfering beams pass through the polarizers twice. The visibility of the fringes depends on the transmittance of the pair of polarizers. The maximum visibility (V_{max}) is observed when the transmittance is maximum i.e. when the polarizer pair is parallel and minimum visibility (V_{min}) is observed when the transmittance is minimum i.e. when the polarizer pair is crossed. Therefore Eqn. (3.20) can be re-written as

$$T_{pair} = \frac{1}{2}\left[V_{\max} V_{\min} \sin^2(\theta) + \frac{1}{2}\left(V_{\max}^2 + V_{\min}^2\right)\cos^2(\theta)\right] \tag{3.21}$$

The extinction ratio is the transmittance/transmitted intensity through a pair of crossed polarizers ($\theta = 90^o$). From Eqn. (3 20), the extinction ratio can be written as

$$H_{90} = T_{pair}(90^o) = \frac{1}{2} V_{\max} V_{\min} \tag{3.22}$$

The open transmittance is the transmittance of a pair of parallel ($\theta = 0^o$) polarizers and is given by

$$H_0 = T_{pair}(0^o) = \frac{1}{4}\left(V_{\max}^2 + V_{\min}^2\right) \tag{3.23}$$

Therefore by measuring the maximum and minimum fringe visibilities of the real fringe system, the extinction ratio and the open transmittance of the polarizer pair can be determined.

3.3.2 Results and Discussion

Three dichroic polarizers working in the wavelength region 400-670 nm are tested using this technique (P_1, P_2 and P_3). All the tested polarizer pairs have a manufacturer specified extinction ratios of 1×10^{-4} and open transmittance of >24%. In all the measurements one of the polarizer is rotated (P_{test}) while keeping the other polarizer (P_{ref}) at the same position. The intensities of the two interfering wave fronts at the detector plane are made equal using neutral density filters in the arms of the interferometer. This ensures that the visibility depends only upon the angle between the polarization directions of the two polarizers (Eqn. 3.18). Visibility is measured by scanning the interferogram both horizontally and vertically at several places. The average of the maximum and minimum intensity values yield the visibil-

ity. Theoretically, visibility varies with angle between the polarizers as shown in Fig 3.22.

The reference polarizer is kept in the transmission arm of the interferometer and the test polarizer is kept in the reflection arm Initially, polarization direction of both the polarizers are kept parallel ($\theta = 0^o$) and the corresponding visibility is measured (V_{max}). This is the maximum obtainable visibility. Then the test polarizer is rotated in steps of 1^o and the corresponding visibilities are measured. When $\theta = 90^o$ a visibility of zero is expected as there is no interference between the two beams because the polarization directions of the two beams are perpendicular to each other, resulting in a uniform intensity distribution across the detector plane. But due to leakage there is a measurable fringe visibility (V_{min}).

Tables 3.8 to 3 13 give the measured fringe visibilities for different polarizer pairs along with the theoretical values and the deviation from the theoretically calculated values. The experimental values are the average of several measurements. The theoretical values are obtained from Eqn. (3.18) with M = 1. A graphical representation of the results in Tables 3.8 to 3.13 is shown in Figures 3.23 to 3.28. Change in the fringe visibility is captured using a CCD camera for $P_2 - P_{ref}$ (P_1) pair for different polarizer angles is shown in Fig. 3.29. At $\theta \sim 90^o$, the fringe pattern cannot be resolved by the CCD camera. Only the scanning using photodiode yielded the fringe visibility. A small shift as well as distortion appeared in the fringe patterns with the change in polarizer angle. This can be seen in Fig. 3.29. This might be due to the non uniformity of the polarizer material or the glass material used as the sandwiching material. It can be seen from the tables and graphs that for all the tested polarizer pairs the visibility is never zero when the polarizer pair is crossed (at $\theta = 90^o$ and $\theta = 270^o$) indicating finite leakage from the polarizers. The extinction ratio, which depends upon the leakage, is calculated from the experimental values using Eqn (3.22) Table 3.14 gives the extinction ratios of the tested polarizer pairs along with the open transmittance calculated using Eqn. (3.23). From the table it can be seen that $P_1 - P_3$ pair is having the lowest extinction ratio. All the pairs have open transmittance $\sim 24\%$ as specified by the manufacturer.

Table 3.8: Change in visibility with polarizer angle for P1(ref) and P2(test) polarizer pair

No.	θ (deg)	Visibility (a.u.)		
		Theoretical	Experimental	Deviation
1	0	1 0000	0.9847	0.0153
2	30	0.8660	0.8719	0.0059
3	60	0.5000	0.5092	0.0092
4	90	0.0000	0.00022	0.0002
5	120	0.5000	0.4897	0.0103
6	150	0.8660	0.8742	0.0082
7	180	1.0000	0.9859	0 0141
8	210	0 8660	0.8761	0.0101
9	240	0.5000	0.5102	0.0102
10	270	0.0000	0.00023	0.0002
11	300	0.5000	0.4902	0.0098
12	330	0.8660	0.8607	0.0053
13	360=0	1.0000	0 9847	0.0153

Table 3.9: Change in visibility with polarizer angle for P1(ref) and P3(test) polarizer pair

No.	θ (deg)	Visibility (a.u.)		
		Theoretical	Experimental	Deviation
1	0	1.0000	0.9804	0.0196
2	30	0.8660	0.8601	0.0059
3	60	0.5000	0.4921	0.0079
4	90	0.0000	0.00023	0.0002
5	120	0.5000	0.4979	0.0021
6	150	0.8660	0.8952	0.0292
7	180	1.0000	0.9812	0.0188
8	210	0.8660	0.8613	0.0047
9	240	0.5000	0.5104	0.0104
10	270	0.0000	0.00022	0.0002
11	300	0 5000	0.5326	0.0326
12	330	0.8660	0.8576	0.0084
13	360=0	1.0000	0.9804	0.0196

Table 3 10: Change in visibility with polarizer angle for P2(ref) and P1(test) polarizer pair

No.	θ (deg)	Visibility (a.u.)		
		Theoretical	Experimental	Deviation
1	0	1.0000	0.9842	0.0158
2	30	0.8660	0.8716	0.0056
3	60	0.5000	0.4873	0.0127
4	90	0.0000	0.00022	0.0002
5	120	0.5000	0.5142	0.0142
6	150	0.8660	0.8572	0.0088
7	180	1.0000	0.9845	0 0155
8	210	0.8660	0.8644	0.0016
9	240	0.5000	0.4906	0.0094
10	270	0.0000	0.00023	0.0002
11	300	0.5000	0.4826	0.0174
12	330	0.8660	0.8481	0.0179
13	360=0	1.0000	0.9842	0.0158

Table 3.11: Change in visibility with polarizer angle for P2(ref) and P3(test) polarizer pair

No.	θ (deg)	Visibility (a.u.)		
		Theoretical	Experimental	Deviation
1	0	1.0000	0.9862	0.0138
2	30	0.8660	0.8636	0.0024
3	60	0.5000	0.4880	0.0120
4	90	0.0000	0.00024	0.0002
5	120	0 5000	0.5098	0.0098
6	150	0.8660	0.8536	0.0124
7	180	1.0000	0.9854	0.0146
8	210	0.8660	0.8897	0.0237
9	240	0.5000	0.4962	0.0038
10	270	0.0000	0.00023	0.0002
11	300	0.5000	0.5142	0.0142
12	330	0.8660	0.8436	0 0224
13	360=0	1.0000	0.9862	0.0138

Table 3.12: Change in visibility with polarizer angle for P3(ref) and P1(test) polarizer pair

No.	θ (deg)	Visibility (a.u.)		
		Theoretical	Experimental	Deviation
1	0	1.0000	0 9807	0.0193
2	30	0.8660	0.8709	0.0049
3	60	0.5000	0.4917	0.0083
4	90	0.0000	0.00022	0.0002
5	120	0.5000	0 4917	0 0083
6	150	0.8660	0.8483	0.0177
7	180	1 0000	0.9815	0.0185
8	210	0.8660	0.8701	0.0041
9	240	0.5000	0.5074	0.0074
10	270	0.0000	0.00022	0.0002
11	300	0.5000	0.5279	0.0279
12	330	0.8660	0.8594	0.0066
13	360=0	1.0000	0.9807	0.0193

Table 3.13: Change in visibility with polarizer angle for P3(ref) and P2(test) polarizer pair

No.	θ (deg)	Visibility (a.u.)		
		Theoretical	Experimental	Deviation
1	0	1.0000	0.9857	0.0143
2	30	0 8660	0.8574	0.0086
3	60	0.5000	0.4907	0 0093
4	90	0.0000	0.00023	0.0002
5	120	0.5000	0.5027	0.0027
6	150	0.8660	0.8617	0.0043
7	180	1.0000	0.9858	0.0142
8	210	0.8660	0.8829	0.0169
9	240	0.5000	0.4931	0.0069
10	270	0.0000	0.00023	0.0002
11	300	0.5000	0.5207	0.0207
12	330	0 8660	0.8529	0.0131
13	360=0	1.0000	0.9857	0.0143

Table 3.14. Calculated extinction ratios and open transmittance of different polarizer pairs

P_{Ref}	P_{Test}	Extinction Ratio (a. u.)$\times 10^4$	Open transmittance (%)
P1	P2	1.1084	24.27
P1	P3	1.0789	24.04
P2	P1	1.1077	24.23
P2	P3	1.1583	24.29
P3	P1	1.0792	24.06
P3	P2	1 1336	24.30

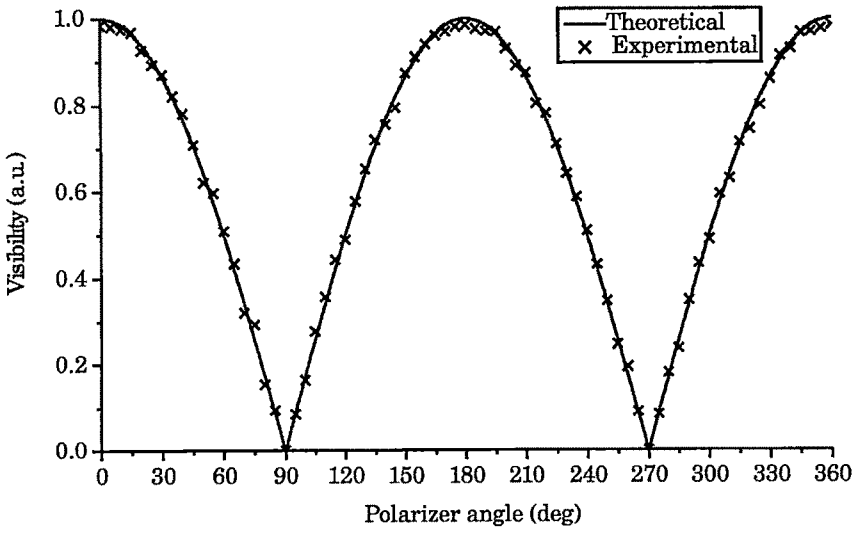

Figure 3 23: Change in visibility with polarizer angle for $P_1(Ref)$ and $P_2(test)$ polarizer pair

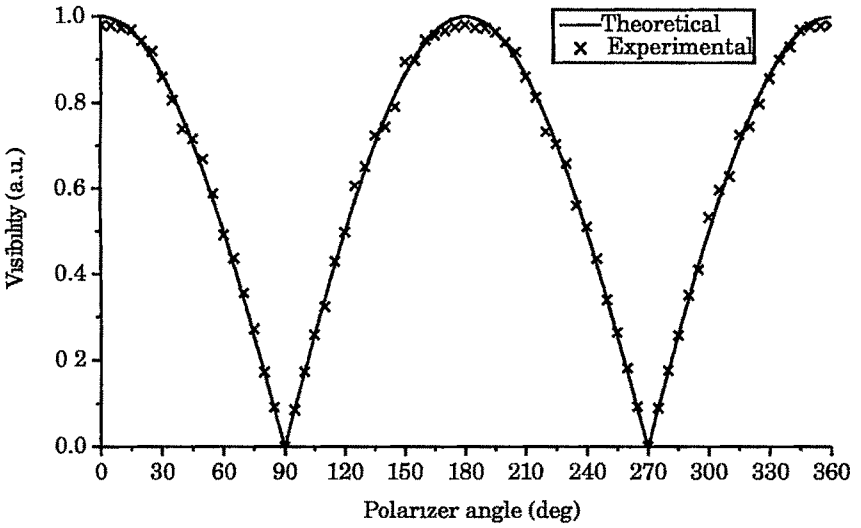

Figure 3.24: Change in visibility with polarizer angle for $P_1(Ref)$ and $P_3(test)$ polarizer pair

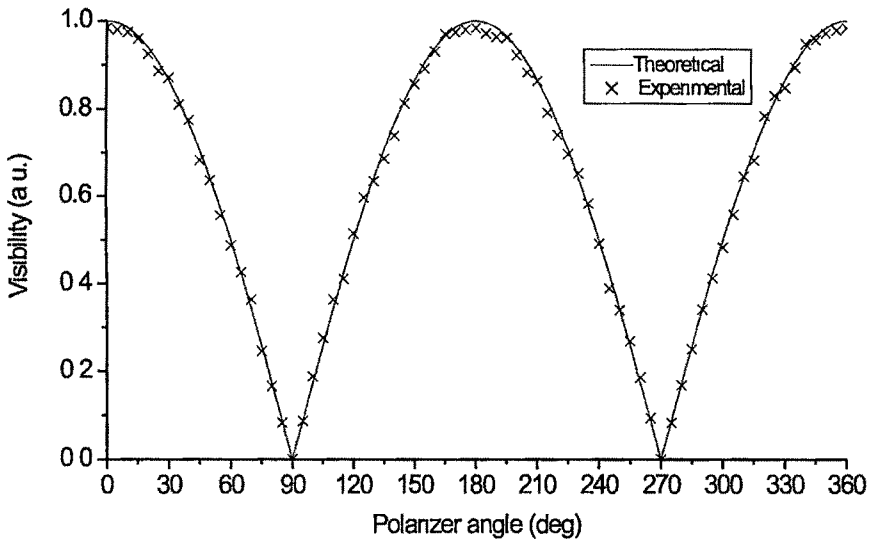

Figure 3.25: Change in visibility with polarizer angle for $P_2(Ref)$ and $P_1(test)$ polarizer pair

The expected maximum visibility is 1, but the obtained maximum visibility is always less than 1 (Table 3.14). This may be due to the non similar transmission/absorption of the two polarizers.

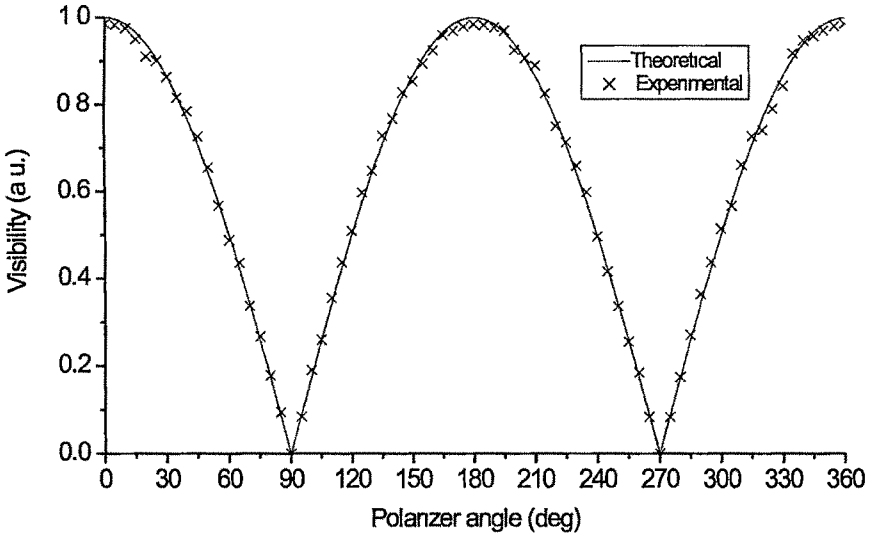

Figure 3.26: Change in visibility with polarizer angle for $P_2(Ref)$ and $P_3(test)$ polarizer pair

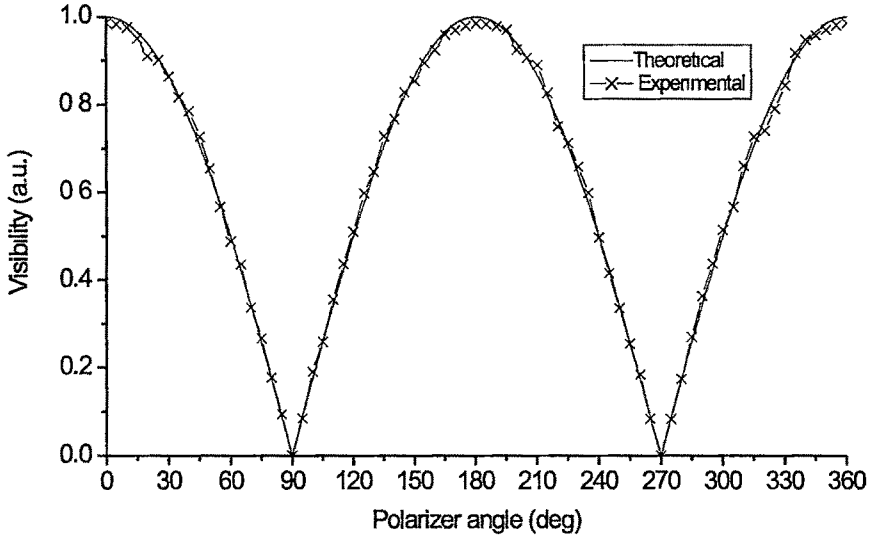

Figure 3.27: Change in visibility with polarizer angle for $P_3(Ref)$ and $P_1(test)$ polarizer pair

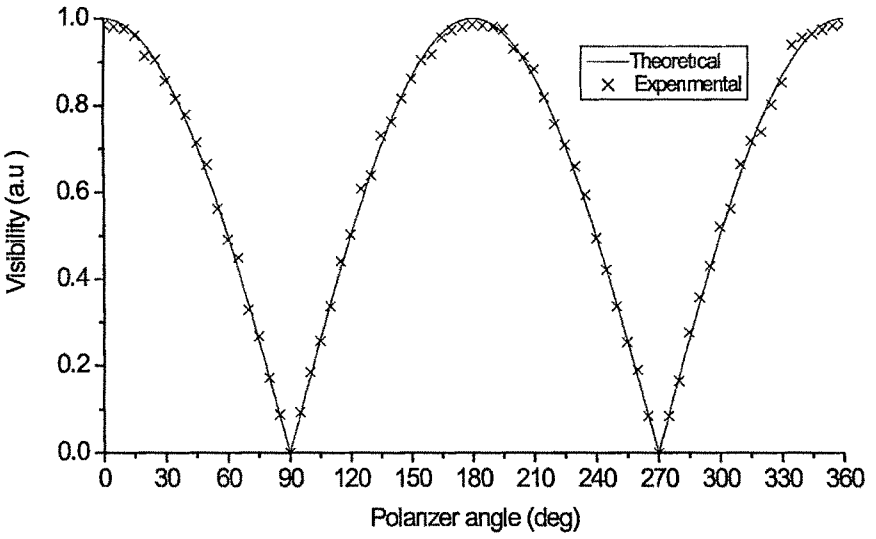

Figure 3.28: Change in visibility with polarizer angle for $P_3(Ref)$ and $P_2(test)$ polarizer pair

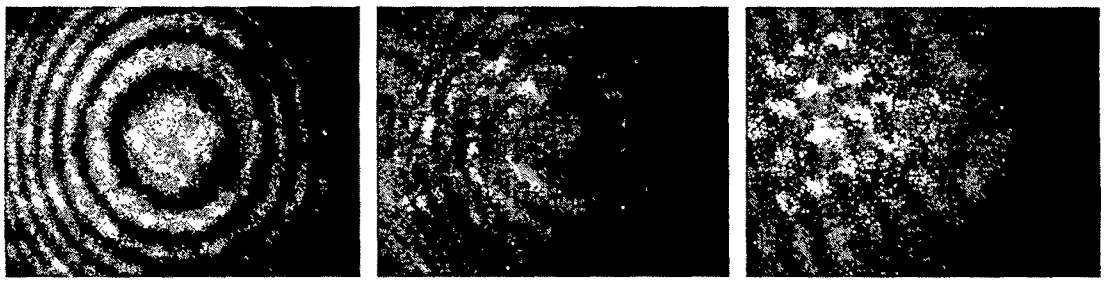

(a) θ=0° (b) θ=60° (c) θ=85°

Figure 3.29: Change in the fringe visibility with polarizer angle for $P_1(Ref)$ and $P_2(test)$ polarizer pair

3.3.3 Error Analysis

The error in measurement of the extinction ratio H_{90} and open transmittance H_0 depends upon the error in measurement of the maximum and minimum visibility V_{max} and V_{min} respectively. The error can be determined by differentiating Equations Eqn. (3.22) and Eqn. (3.23) partially with respect to V_{max} and V_{min}.

$$dH_{90} = \frac{H_{90}\, dV_{\min} + V_{\min}^2\, dV_{\max}}{V_{\min}} \tag{3.24}$$

Suppose the error in finding V_{max} and V_{min} is 2.5 % and $V_{max} = 0.9850$ and $V_{min} = 0.00022$ and the expected $H_{90} = 1 \times 10^{-4}$, then the error in finding H_{90} is $\sim 0.07 \times 10^{-4}$. Differentiating Eqn. (3 23) partially with respect to V_{max}, the error in determining the open transmittance can be determined. The second term in Eqn. (3 23) can be safely ignored as $V_{min} \ll V_{max}$.

$$dH_0 = \frac{V_{\max}\, dV_{\max}}{2} \tag{3.25}$$

For example if the error in finding V_{max} is 2.5% and $V_{max} = 0.9850$ then the error in finding the open transmittance H_0 is 0.012.

3.3.4 Conclusion

Michelson interferometer is used to test linear polarizers very accurately both qualitatively and quantitatively. The qualitative study of the polarizer pair can be made by analyzing the resulting fringe systems. It is found that in some cases the fringe pattern shifted with polarizer angle. This can be attributed to the non-uniformity of either the polarizer or the glass material sandwiching it. Since the fringe quality depends upon the polarizers, this method gives the quality of the polarizer materials, making it more advantageous than other methods. Quantitatively speaking, the extinction ratios and the open transmittance of the polarizer pairs are found using this method very accurately. The error in finding H_{90} is $\sim 7\%$ and the error in finding H_0 is $\sim 1\%$.

3.4 Beamsplitter testing with Michelson Interferometer

Beamsplitters play an important role in most of the sensitive optical experiments like interferometry, holography, phase conjugation etc. For all these experiments, proper splitting of the incident beam into required beam ratios is very essential and for that proper design of a beamsplitter is important. The beamsplitters consist of a thin window, on each side of, which is deposited, a different type of coating. The first surface is coated with an all-dielectric film having partial reflection properties either

in the visible, ultraviolet or the near-infrared spectrum and the second surface has an antireflection coating optimized for 45°(Fig. 3.30)[85, 101] . One can also design non polarizing beamsplitters, where the polarization characteristics of incident laser radiation is maintained in the reflected and transmitted beams and it also splits the incident laser energy into either 50.50 or 75:30 regardless of the incident state of polarization. In such non-polarizing beamsplitters if the coatings (reflection and antireflection) are proper then 50% or 70% of the incident beam should be transmitted and the remaining 50% or 30% should be reflected. On the other hand, if the reflection and anti reflection coatings are not proper then such (non polarizing) commercially available beamsplitters, split the incident beam from the laser source into more than one along transmission direction and reflection direction each, thus resulting in unequal and unspecified (neither 50:50 or 70:30) distribution of incident laser energy (Fig. 3.31). The effect of such splittings will not be prominent unless sensitive optical experiments like photorefractive effect, phase conjugation etc are done where the energy of laser beams plays an important role. Also, it is very difficult to notice this effect unless an unexpanded laser beam is allowed to fall on such a beamsplitter before spatial filtering However, in a Michelson Interferometric experimental set up if a diverging laser beam falls on such a beamsplitter, then for unequal arms length two or more sets of circular fringes, instead of one set of circular fringes are obtained.

In many of the commercial beamsplitters the reflection and anti-reflection coatings are not proper and due to this the splittings of incident laser beam for a 50:50 or 70:30 type beamsplitter may not be strictly one along transmission and reflection directions respectively. Earlier a method was developed to test the quality of beamsplitters using temporal coherence[5, 56, 102] of a laser beam in a Michelson Interferometer experimental set-up[103] Another method to test beamsplitter using photorefractive effect was also developed[104] In this method diffraction efficiencies of the induced gratings were used to find out the beams ratios[104] But here measurement of the ratios of all the beams from the beamsplitter was not possible. So an accurate quantitative method to test beamsplitters has to be developed. In this section a modification to the beamsplitter testing using Michelson interferometer is proposed to yield the beam ratios of all the beams interfering at the detector plane. The beam ratios of the interfering beams are calculated from the visibility of the resulting interference fringes

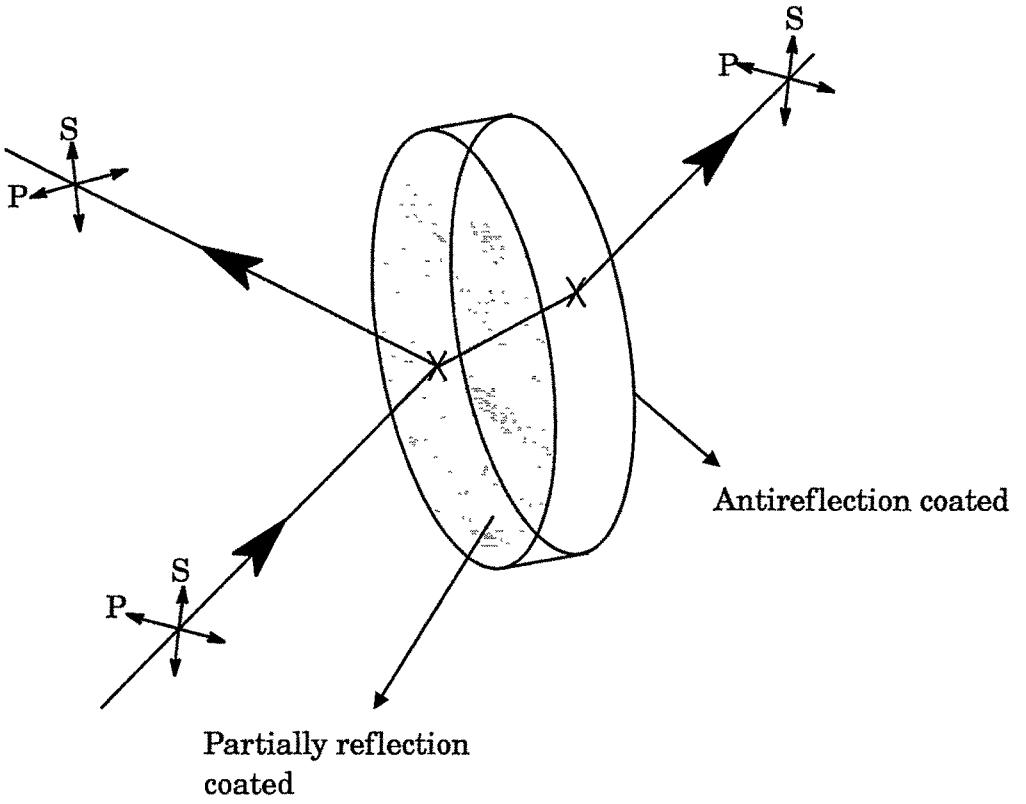

Figure 3.30: Ideal beamsplitter

The visibility of the fringe systems is determined by scanning the fringe pattern with a photodiode.

3.4.1 Experimental Procedure and Theory

Consider a typical Michelson Interferometric set-up with a laser source as shown in Fig. 3.32. The laser beam (10 mW, $\lambda = 632.8$ nm), is spatially filtered and is allowed to fall on the beamsplitter which, is to be tested The beamsplitter splits this diverging laser beam into two. The partially transmitted beam travels to the mirror M1 and the partially reflected one from the beamsplitter travels to mirror M2. These two beams will be reflected back to the beamsplitter by the respective mirrors which, finally interfere at the detector plane nearer to the beamsplitter to give real circular fringe pattern. For an ideal beamsplitter (Fig. 3.31), the Michelson interferometric theory holds well since, the interference takes place between only two time-delayed wave fronts (one along transmission and the other along

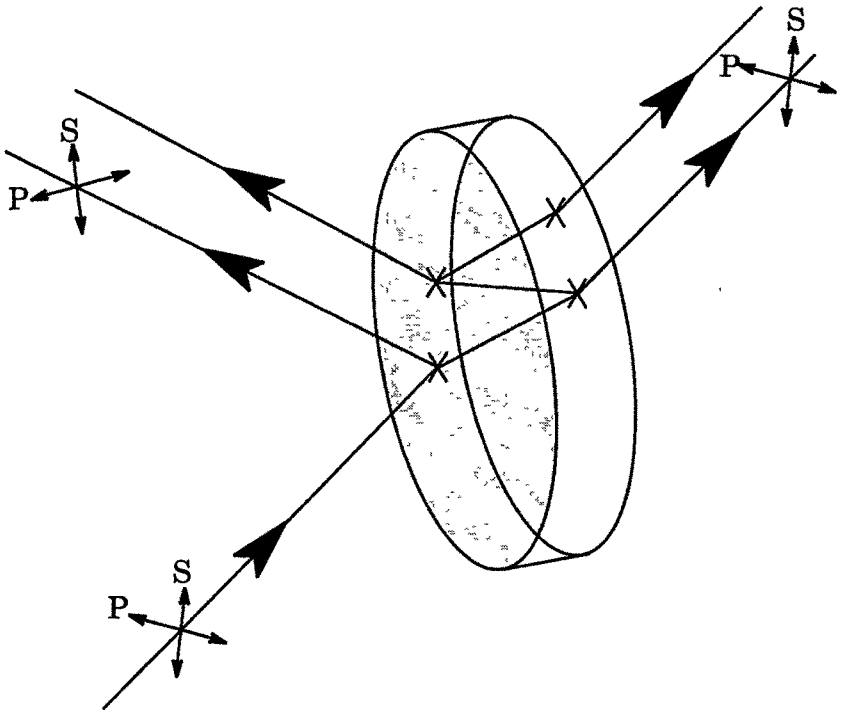

Figure 3.31: Improperly coated beamsplitter

reflection). On the other hand, if the beamsplitter splits the incident beam into more than one along transmission and reflection directions respectively as shown in Fig. 3.31, then the theory has to be modified. Assume that a spherical wavefront (amplitude varies inversely with the radius R of the wavefront) from the pinhole of the spatial filtering assembly falls on such imperfectly coated beamsplitter which splits the incident laser beam into two along transmission and two along reflection. Let us assume that $(E_0/R)\, e^{i\phi}$ is a diverging laser beam incident on such a beamsplitter. Then $(E_{r1}/R_{r1})\, e^{i\phi_{1r}}$ and $(E_{r2}/R_{r2})\, e^{i\phi_{r2}}$ are the beams reflected towards the direction of mirror M1 and $(E_{t1}/R_{t1})\, e^{i\phi_{t1}}$, $(E_{t2}/R_{t2})\, e^{i\phi_{t2}}$ are the beams transmitted by the beamsplitter towards the direction of mirror M2 (ϕ's represents the phases of the diverging beams). The mirrors M1 and M2 will reflect back these wave fronts to the beamsplitter and now at the detector plane the total intensity of the interference pattern becomes,

$$I_T = \left(\frac{E_{r1}}{R_{r1}}\, e^{i\phi_{r1}} + \frac{E_{t1}}{R_{t1}}\, e^{i\phi_{t2}} + \frac{E_{r2}}{R_{r2}}\, e^{i\phi_{r2}} + \frac{E_{t2}}{R_{t2}}\, e^{i\phi_{t2}}\right)^2 \tag{3.26}$$

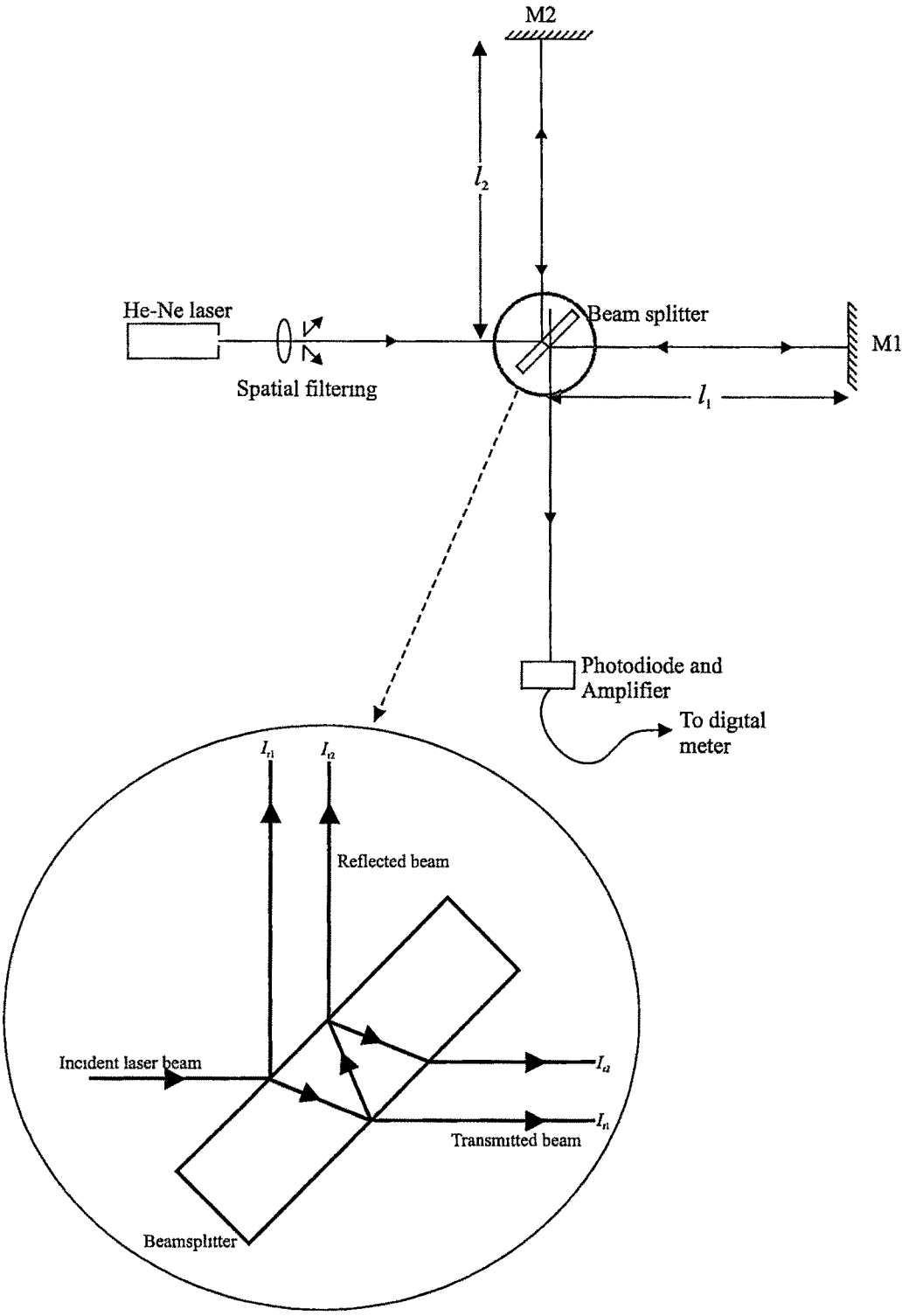

Figure 3.32: Experimental setup for the testing of the beamsplitter

$$I_T = I_{r1} + I_{t1} + I_{r2} + I_{t2} + 2\sqrt{I_{r1}I_{t1}}\cos\varphi_{r1t1} + 2\sqrt{I_{r2}I_{t2}}\cos\varphi_{r2t2} + 2\sqrt{I_{r1}I_{t2}}\cos\varphi_{r1t2} + 2\sqrt{I_{r2}I_{t1}}\cos\varphi_{r2t1} \quad (3.27)$$

Where φ's are phase differences between the time delayed interfering beams From Eqn. (3.27) it can be seen that many interference patterns can exist simultaneously because of the shift of the two interfering beams due to shearing of the wave front. Eqn. (3 27) can be re-written in terms of the visibility of the interference fringes as

$$I_T = I_B\left(1 + V_1\cos\varphi_1 + V_2\cos\varphi_2 + V_3\cos\varphi_3 + V_4\cos\varphi_4\right) \quad (3.28)$$

where $I_B = I_{r1} + I_{t1} + I_{r2} + I_{t2}$ is the background intensity.

$$V_1 = \frac{2\sqrt{I_{r1}I_{t1}}}{I_B} \quad , \quad V_2 = \frac{2\sqrt{I_{r2}I_{t1}}}{I_B} \quad , \quad V_3 = \frac{2\sqrt{I_{r2}I_{t2}}}{I_B} \quad , \quad V_4 = \frac{2\sqrt{I_{r1}I_{t2}}}{I_B} \quad (3.29)$$

are the visibilities of the individual fringe systems. Where one fringe system is present, the intensity distribution due to other acts as the background intensity, reducing the visibility. The experimental geometry shown in Fig. 3.32 will yield real fringes when a point source is used. These real fringes can be observed on a screen. By scanning the interference fringes with a photodiode the visibility can be determined. Visibility of the fringes gives the intensity ratios of the interfering beams.

3.4.2 Results and Discussion

Three broad band non-polarizing beamsplitters with 50:50 splitting specifications are investigated using this method. The setup in Fig. 3.32 is used with different beamsplitters. The mirrors are adjusted to obtain circular fringes at the screen. The distance between the beamsplitter and mirror M1 is kept at 700 mm. Mirror M2 is moved to change the path length difference (Δx) between the two beams. In two of the investigated beamsplitters (BS-A, BS-B), the incident beam is split into two overlapping beams along the reflection direction (because of back reflection from the second surface) and one along the transmission direction resulting in two individual fringe systems The third beamsplitter (BS-C) is having a wedge and so the beams do not overlap at the detector plane and resulting in a single fringe system.

The obtained fringe systems are spatially separated. This can be understood from the fact that the interference occurs between 1) the spherical wave front from the reflection and transmission 2) spherical wave front internally reflected (sheared) and the transmitted wave front. Figures 3.33a to 3.33c shows the change in the fringe systems for BS-A with change in path difference when a He-Ne source of 632.8 nm is used. Two fringe systems existing simultaneously can be seen in Fig. 3.33a and 3.33b. It can also be seen that as the path difference is decreased the spatial separation between the fringe systems increase and finally when the path difference ~ 0 only one of the fringe systems occupy the field of view. By adjusting the mirrors the second fringe system can be brought into the field of view. Fig. 3.34 shows the two fringe systems for BS-A when $x = 5$ mm. It can be seen that the visibility of the secondary fringe system (due to I_{t1} and I_{r2}) is less indicating interfering beam ratios $\ll 1$. This happens because the second reflected beam is of very low intensity and reflected beam from the front surface acts as a background illumination reducing the visibility.

Fig. 3.35 shows the variation in fringe system with path difference for BS-C. It can be seen that even for large path differences, there is only a single fringe system indicating that there is no overlap. The separation between the fringe systems are measured as a function of path difference. Fig. 3.36 shows the plot for the change in fringe separation with path difference of the interfering beams for BS-A and BS-B. The screen is placed 650 mm from the beamsplitter. The separation at x=0 is obtained by extrapolating the data for large path differences. From these plots, it can be seen that the separation increases with decrease in path difference.

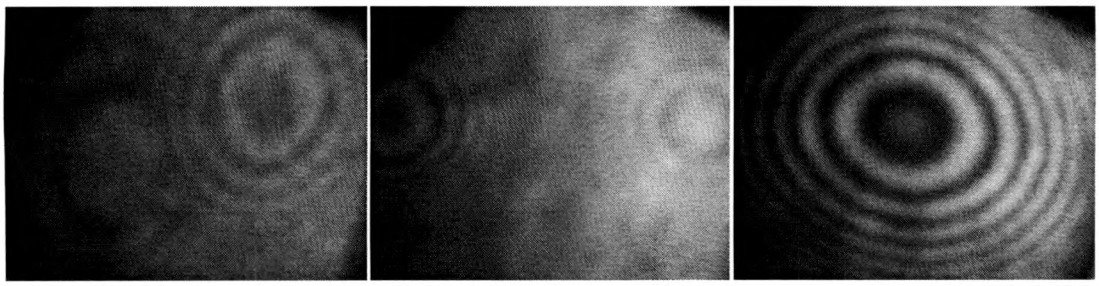

(a) Δx=75mm (b) Δx=50mm (c) Δx=5mm

Figure 3.33: Interference patterns for different path differences for BS-A

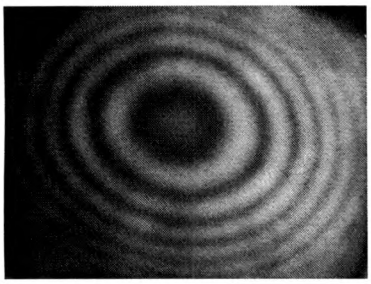

(a) Interference between I_{t1} and I_{r1}

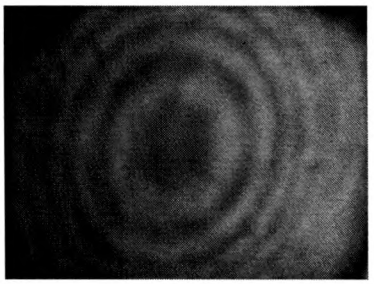

(b) interference between I_{t1} and I_{r2}

Figure 3.34: Two separate interference fringe systems at the detector plane when Δx = 5 mm

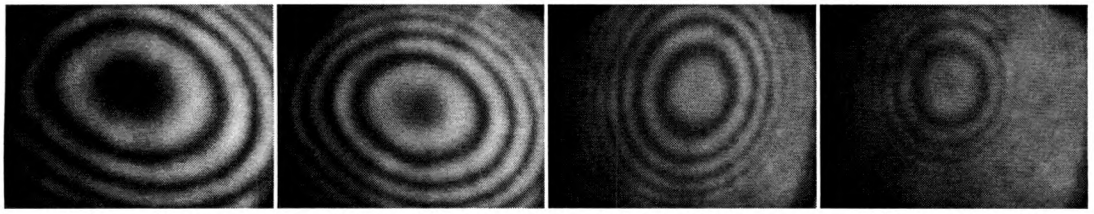

(a) Δx=5mm (b) Δx=25mm (c) Δx=75mm (d) Δx=100mm

Figure 3.35: Interference patterns for different path differences for BS-C

3.4.3 Beam ratio calculations

Visibilities of the two resulting fringe systems when $\Delta x \sim 0$ is used to calculate the intensity ratios of the three beams resulting in interference at the detector plane. For a beamsplitter splitting the beam into two along the reflection and one along the transmission direction, the intensity equation (Eqn. 3.28) can be rewritten as

$$I_T = I_{t1} + I_{r1} + I_{r2} + 2\sqrt{I_{r1}I_{t1}}\cos\varphi_{r1t1} + 2\sqrt{I_{r2}I_{t1}}\cos\varphi_{r2t1} \tag{3.30}$$

The visibility of the two individual fringe systems is then

$$V_1 = \frac{2\sqrt{I_{r1}I_{t1}}}{I_{t1} + I_{r1} + I_{r2}} \tag{3.31}$$

and

$$V_2 = \frac{2\sqrt{I_{r2}I_{t1}}}{I_{t1} + I_{r1} + I_{r2}} \tag{3.32}$$

with $I_{t1} + I_{r1} + I_{r2}$ as the background illumination

The visibilities of the fringe systems depend upon the beam intensities of the two interfering beams as well as on the intensity of the third beam. The presence of

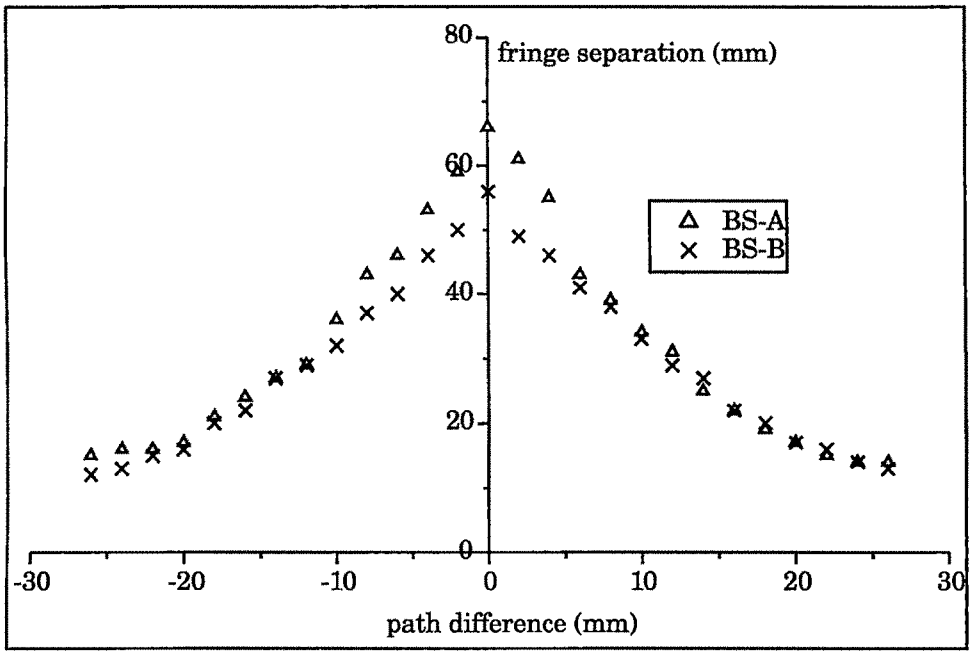

Figure 3.36: : Change in fringe separation for with path difference

the third beam therefore reduces the fringe visibility (Eqn. (3.31) and Eqn. (3.32)). The visibility of the beams is measured by scanning each of the fringe system with a photodiode and finding the minimum and maximum intensities. Dividing Eqn. (3.31) by Eqn. (3 32), the beam ratios of the two reflected beams can be obtained.

$$\frac{I_{r1}}{I_{r2}} = \left(\frac{V_1}{V_2}\right)^2 \tag{3.33}$$

Using Eqn (3.33) in (3.31) and (3.32), the beam ratios of the transmitted and reflected beams can be calculated. Table 3.15 gives the calculated beam ratios for all the tested beamsplitters. It can be seen that for BS-A and BS-B, the fringe visibility is low compared to BS-C, where only one reflected and transmitted beam interfere at the detector plane. Assuming that there is no energy loss at the beamsplitter i.e. the beam is split into three only, the percentage of the reflected and the transmitted beams at the detector content can be calculated. Table 3.16 gives the percentage of the reflected and transmitted beams at the detector plane. It can be seen that BS-C has beam ratios closest to the manufacturer specified values. BS-B does split the beam slightly better than BS-A as its primary beam ratio ($I_{t1} : I_{r1}$) is nearer to 1 and its secondary beam ratio ($I_{t1} : I_{r2}$) is higher compared to BS-A. Primary beam ratio nearer to 1 and high secondary beam ratios yield better visibility of the interference

fringes. The energy loss due to multiple reflections in the beamsplitter is more in BS-A

Table 3.15· Calculated beam ratios

Beamsplitters	Visibilities of individual		Beam ratios of different beams fringe systems (a.u.)		
	V_1	V_2	I_{t1}/I_{r1}	I_{t1}/I_{r2}	I_{r1}/I_{r2}
BS-A	0.908	0 385	1.64	9.17	5 56
BS-B	0.938	0 329	1.39	11.35	8 13
BS-C	0.998	—	1.13	—	—

Table 3.16· Calculated beam percentages at the detector plane

Beamsplitters	% of the total		
	I_{t1}	I_{r1}	I_{t1}
BS-A	58 15	35.46	6.39
BS-B	55 31	39.79	4 90
BS-C	53 06	46.94	—

3.4.4 Conclusion

A method is developed to calculate the beam ratios of interfering beams from a beamsplitter. The method developed is very accurate as the beam ratios are derived from the interference fringes formed by the beams, rather than directly measuring the beam intensities. Direct measurement will only yield the total intensity of the overlapped beams rather than their individual intensities. The method can also be used to determine the loss of energy due to multiple reflections inside the beamsplitter.